Photoexcited Carrier Dynamics in Mixed Halide Perovskites: A Morphological Perspective

By

Eric M. Talbert

Thesis
Submitted to the Faculty of the
Graduate School of Vanderbilt University
in partial fulfillment of the requirements
for the degree of

MASTER OF SCIENCE

in

Chemical Engineering

August 2016
Nashville, Tennessee

Approved: Date:

_____ _____
Rizia Bardhan, Ph.D.

_____ _____
G. Kane Jennings, Ph.D.

ACKNOWLEDGEMENTS

This work was made possible by the gracious help and mentorship of many close friends and colleagues. My thesis advisor, Dr. Rizia Bardhan, has provided unwavering focus and direction in leading this project, and challenged me to be organized and professional in all of my data analysis and presentation. My undergraduate assistants, Zach DeBra and Chris McDonald, performed several experiments to advance the planar perovskite project. My labmates, particularly Will Erwin, Holly Zarick, and Naiya Soetan, have supported me throughout this work, contributing valuable discussion and encouragement along the way. The chemical engineering department faculty, especially Dr. Kane Jennings and Dr. Doug LeVan, have also shown incredible support, constantly making me feel welcome as a professional and scholar. Along with the other graduate students, I would like to thank all of you for enriching this project and my experience in graduate school.

I would also like to thank our collaborators: Noah Orfield and Kemar Reid for running tr-PL experiments under the direction of Dr. Sandra Rosenthal, Dr. James McBride for helping locate perovskite nuclei in STEM-EDS, Wei Li for running focused ss-PL spectra under the direction of Dr. Jason Valentine, and Dr. Abdelaziz Boulesbaa for leading TAS experiments at Oak Ridge National Lab in the research group of Dr. David Geohegan. These materials characterization experts, now friends and colleagues, have exposed me to many fascinating optical techniques, providing essential insights to guide this work. I also thank the Vanderbilt Institute of Nanoscale Science and Engineering for teaching me to effectively operate a wide range of characterization equipment, and for providing funding through the VINSE fellowship. Finally, I acknowledge Vanderbilt startup funds for making this project and experience possible.

TABLE OF CONTENTS

Page

LIST OF FIGURES AND TABLES

CHAPTER 1

Introduction

Hybrid organic-inorganic perovskites have made tremendous strides in the past five years as a promising absorber material for next generation perovskite solar cells (PSCs), improving in device efficiency from 3.8% in 2009[1] to over 22% in 2016.[2-6] This vast improvement in performance is due both to improved synthesis of defect-free perovskite films and to the engineering of electron- and hole-selective contacts that enable efficient charge separation. While a few startup companies seek to commercialize solar cells based on methylammonium lead iodide ($CH_3NH_3PbI_3$) as early as 2017, fundamental research on perovskites is still growing with the goal of elucidating the underlying mechanisms of absorption and charge transport that give hybrid perovskites such intriguing potential. The work presented in this thesis seeks to translate phenomenological observations into morphological insights for directing the synthesis of $CH_3NH_3PbI_3$-type perovskites.

This class of perovskites derives its novelty as an absorber material for solar cells from its unique combination of strong light absorption, low exciton binding energy, and efficient charge transport. Upon illumination of this semiconductor absorber, incident photons with energy exceeding the bandgap (1.55-1.6 eV for $CH_3NH_3PbI_3$) generate excitons, or an electron-hole pairs, by exciting a valence electron in the perovskite to the conduction band. The bandgap in perovskite is almost perfectly direct, achieving efficient absorption without the necessity of phonon coupling and minimizing irreversible energy losses.[7] Because the photogenerated excitons are of the Wannier-Mott type, the exciton binding energy is sufficiently low (estimates range between 2 and

55 meV for $CH_3NH_3PbI_3$; for reference, k_bT is 25.7 meV at 25 °C)[8, 9] that the electrons and holes readily split and migrate toward their respective electrodes. By substituting any of the A^+, B^{2+}, or X^- components of the ABX_3 perovskite crystal, one can engineer the lattice to be pseudocubic, tetragonal, or stacks of two-dimensional sheets.[10] This structural variation affects the optoelectronic properties as well, enabling tunability of the perovskite bandgap, exciton binding energy, and carrier diffusion lengths.[11]

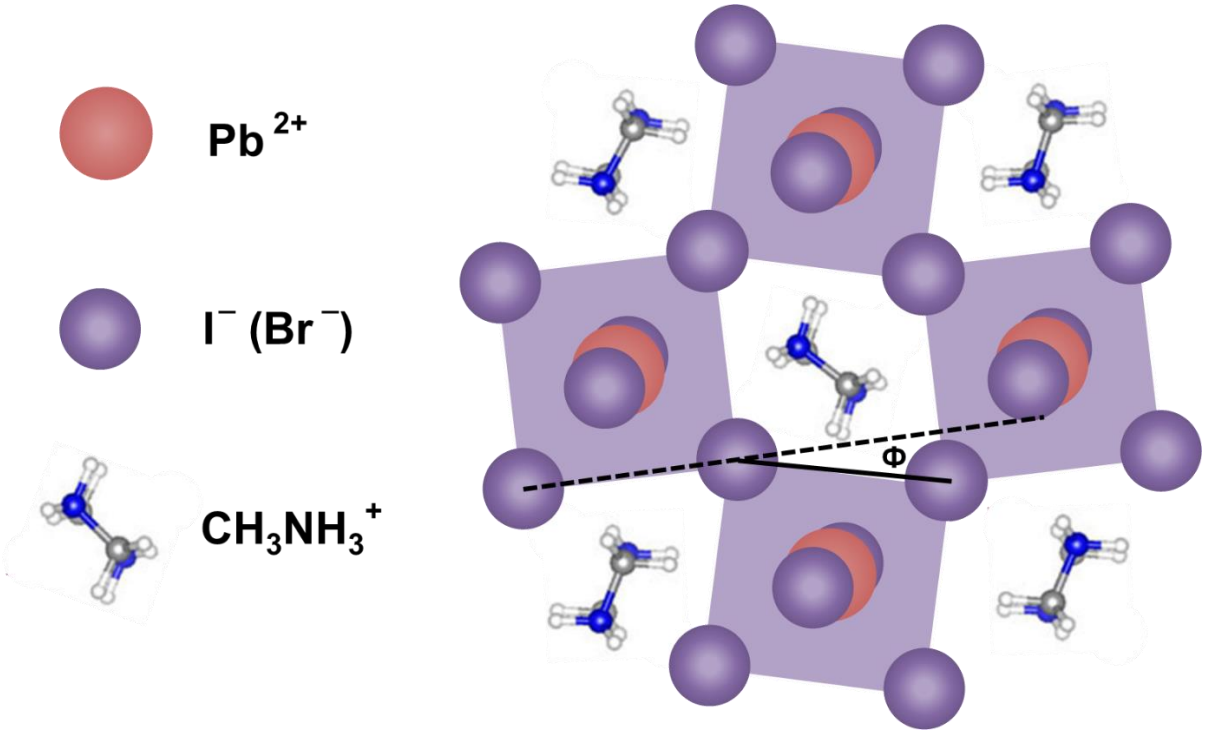

Figure 1.1: Crystal structure of hybrid perovskite $CH_3NH_3PbI_3$. When Br is substituted for I, the lattice offset Φ decreases from 15° to approximately 0°. Methylammonium cations rotate freely in their octahedral holes.

Methylammonium lead iodide has emerged as the leading perovskite candidate for future solar cells due to its strong broadband absorption below its direct bandgap of 1.6 eV, facile synthesis from solution- and/or vapor-phase processing, and long diffusion lengths for

photogenerated electrons and holes. $CH_3NH_3PbI_3$ films are readily synthesized using a variety of one-step and two-step approaches. In the one-step synthesis, a precursor solution of PbI_2 (or $PbCl_2$) and CH_3NH_3I salts dissolved in a polar solvent is generally spin-coated onto the substrate; $CH_3NH_3PbI_3$ crystallizes as the acceleration of rotation drives solvent evolution, and the film is further annealed to remove all residual solvent. However, major differences in grain size and film quality can arise from variations in PbI_2 and CH_3NH_3I concentration (especially deviations from the stoichiometric ratio), substitution of the precursor solvent, or use of an antisolvent treatment to induce crystallization.[12, 13] In the two-step synthesis, PbI_2 is spin-coated first, either onto a planar surface or more commonly onto a high surface area, mesoporous TiO_2 substrate. The substrate is then immersed in a solution or vapor rich in CH_3NH_3I, in which CH_3NH_3I is incorporated within seconds to form perovskite due to the high diffusivity of CH_3NH_3I in $CH_3NH_3PbI_3$. The remarkable mobility of $CH_3NH_3^+$ and I^- ions through the perovskite lattice may contribute to the unparalleled absorption and charge transport of $CH_3NH_3PbI_3$-type materials,[2, 4, 14] but much remains to be uncovered regarding structural effects on the absorption and charge transport mechanisms.

Despite the advantages as a solar energy material, degradation of $CH_3NH_3PbI_3$ in humid atmosphere has remained a major obstacle for the commercialization of $CH_3NH_3PbI_3$-based devices.[15-17] Approaches to surmount this challenge have included encapsulation of $CH_3NH_3PbI_3$ devices in polymers,[18, 19] addition of water-impermeable electron- or hole-selective layers,[18, 20, 21] or controlled doping of $CH_3NH_3PbI_3$ perovskites with bromide ions.[22-27] The addition of bromide reduces the perovskite lattice parameter due to its smaller ionic radius, which restricts the diffusion of water into the methylammonium vacancies and improves the moisture stability of the perovskite.[22] As bromide concentration is increased, the lattice structure shifts from tetragonal to

cubic, decreasing the angle of offset of the lead halide octahedra (from 15° for $CH_3NH_3PbI_3$ toward 0° for $CH_3NH_3PbBr_3$).[11, 22] The decreased angle of offset promotes linear charge transport, increasing the diffusion length/conductivity of carriers in the perovskite. Doping with Br ions also provides an avenue to tune the bandgap of the perovskite for broadband light absorption and increased open circuit voltages.[28] Although the increased bandgap with Br doping of $CH_3NH_3PbI_3$ reduces the light absorption, several studies have suggested that $CH_3NH_3Pb(I_{1-x}Br_x)_3$ perovskites with Br composition, x, between 0 and 0.33 provide an optimal balance between light absorption, charge transport, and moisture stability.[23-26]

This thesis focuses on the effect of added bromide ions to the structural and optoelectronic properties of $CH_3NH_3Pb(I_{1-x}Br_x)_3$ perovskites within the tetragonal regime ($0 \leq x \leq 0.33$). In the next chapter, I will discuss the morphologies of $CH_3NH_3Pb(I_{1-x}Br_x)_3$ films synthesized by various spin-coating procedures in both planar and mesoporous geometries. While grain size and film thickness vary greatly depending on precursor formulations, the grain-scale morphology is independent of bromide content, an important consideration when comparing absorption and charge transport across bromide concentrations. Chapter three provides a discussion of charge transport with respect to bromide content and grain morphology in planar $CH_3NH_3Pb(I_{1-x}Br_x)_3$ films, focusing on evidence of electron-hole recombination extracted from steady-state (ss-PL) and time-resolved (tr-PL) photoluminescence experiments. A comparison of absorbance and fluorescence spectra reveals that the fluorescence has a lower energy than would be expected from bulk absorbance, hinting that recombination is likely driven by variations in bromide composition within perovskite grains. Finally, chapter four introduces ongoing work in probing the absorption dynamics of mesoporous titania-supported $CH_3NH_3Pb(I_{1-x}Br_x)_3$ films with transient absorption spectroscopy (TAS). While charge injection lifetimes are constant across bromide compositions,

carrier thermalization lifetimes decrease with increasing bromide content, indicating that added bromide promotes phononic coupling and subsequent heat transfer. These results conclude that grain-scale and lattice-scale morphology have a profound effect on optoelectronic performance, especially for $CH_3NH_3Pb(I_{1-x}Br_x)_3$, which is important to consider in the engineering of future solar devices.

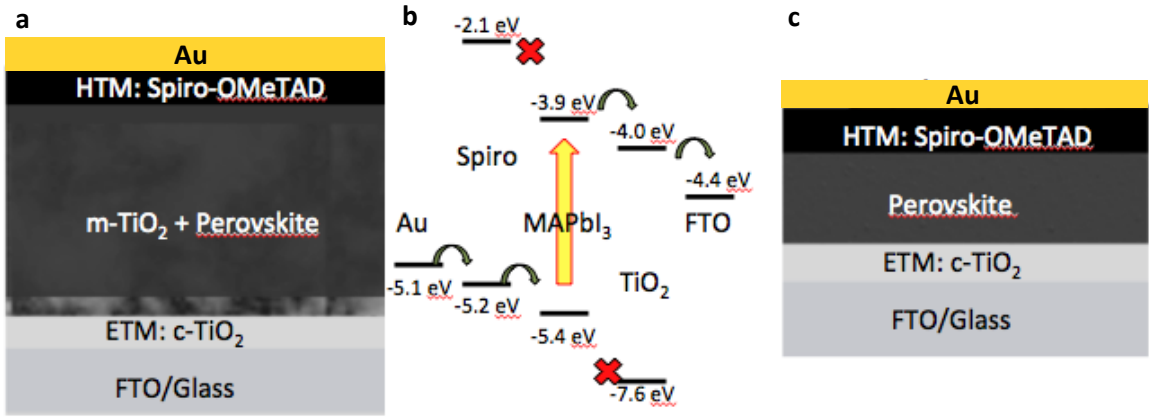

Figure 1.2: Device schematics for (a) mesoporous and (c) planar perovskite solar cells. Typical electron- and hole-selective contacts with close work function alignment control the direction of electron (and hole) transport, as shown in the energy level diagram in (b).

CHAPTER 2

Morphological Engineering of $CH_3NH_3PbI_3$-like Perovskites

Similar to other semiconductor electronics, perovskite solar cell performance strongly relies on the minimization of defects and pinholes in each layer of the layered device. Thus, it is imperative to design the perovskite active layer with maximum smoothness and coverage. Early on, the largest gains in perovskite solar cell efficiency came from templating the perovskite crystal growth with a mesoporous scaffold of TiO_2 or Al_2O_3. Mesoporous TiO_2 gives the added benefit of a high surface area for injection of photogenerated electrons. More recently, free-standing planar perovskite films have overtaken the mesoporous architecture in device efficiency, in part because of the extensive research on the optoelectronic properties of stand-alone perovskite crystals. This chapter provides a detailed look at the grain structure of $CH_3NH_3Pb(I_{1-x}Br_x)_3$ perovskites in both planar and mesoporous architectures, establishing the necessary control morphologies for our optoelectronic studies.

A. *Planar Perovskites: A Comparison of Grain Structures*

A wide range of solution-processed[29-31] and vapor-assisted[12, 32-34] techniques have been reported to achieve smooth yet highly crystalline planar perovskite films. An unintended consequence of this synthetic variety is that the morphological differences between perovskite films often goes undiscussed. The structural discussion is often overlooked in literature, and some synthetic procedures as reported could not possibly yield the pristine perovskite films depicted in published SEM micrographs. Besides a strong reliance on film uniformity, planar perovskite

devices are particularly prone to impurities. As most planar depositions involve a one-step spin-coating procedure, any impurity in PbI_2, CH_3NH_3I, or CH_3NH_3Br salts is more likely to be immobilized within the film, introducing a lattice defect and/or a recombination trap site.[35] These reagents were purchased at the highest purity available (PbI_2, Sigma Aldrich, 99.9999%; CH_3NH_3I and CH_3NH_3Br, Dyesol, 99%) to minimize impurity defects. The following paragraphs detail the differences in film quality and grain size for a variety of precursor solvent and antisolvent processing conditions.

Early in our lab's optimization of planar $CH_3NH_3PbI_3$-type films, we realized that the key to smooth, pinhole-free crystallization is the use of an antisolvent extraction technique. Simply

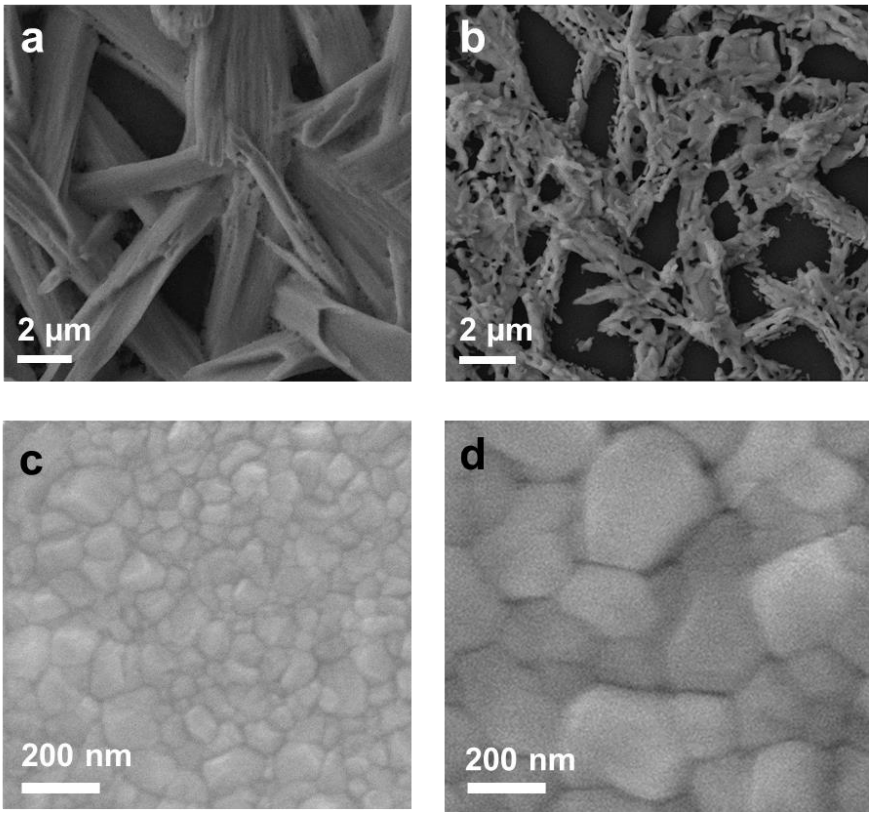

Figure 2.1: SEM micrographs of $CH_3NH_3PbI_3$ perovskite crystals from (a) DMF, (b) 3:7 v/v DMSO:GBL, (c) DMF with toluene antisolvent treatment, and (d) DMSO:GBL with toluene antisolvent treatment.

spin-coating 200 µL of 40 wt% stoichiometric precursor in DMF at 4000 rpm yielded a splatter of large rod-shaped crystals. Substituting a 3:7 v/v mixture of DMSO:GBL for DMF as suggested by Jeon *et al*,[12] the development of discrete grains reduced the roughness but made no progress toward complete coverage. The film quality improved remarkably when 400 µL of toluene was drizzled during the spin ramp, and a smooth film was produced regardless of solvent when this antisolvent was added as the glass substrate was spinning at approximately 2000 rpm. At this speed, the film is a suspension of nascent perovskite crystals in precursor solvent, slowly crystallizing as solvent is centrifuged outward. When the toluene antisolvent is pipetted on top of this suspension, perovskite crystals crash out due to their insolubility in toluene and deposit in the same relative positions as they were suspended in the thin liquid film. The precursor solvent is extracted by the toluene and washed away as the spin speed increases. The resultant continuous film of perovskite crystals is annealed at 100 °C for 1 h to remove any residual solvent. SEM images of $CH_3NH_3PbI_3$ produced with and without the antisolvent treatment highlight the importance of constraining crystal growth during perovskite film synthesis (Figure 2.1).[6, 12, 36]

The stark difference in grain size between DMF-processed and DMSO:GBL-processed perovskite films is attributed to the level of complexation of the precursor solvent with PbI_2. It has been proposed that DMSO's polar structure promotes the stable formation of a Pb-O bond between PbI_x species and DMSO in solution.[37] The oxygen atom in DMF is stabilized by the amide group, forming a weaker complex with PbI_x ionic species. Wu et al. predicts that the difference in Pb-O bond length (and thus stability) drives DMSO-containing precursor solutions to nucleate perovskite crystals at room temperature whereas DMF-based precursor solutions experience negligible nucleation. Larger nuclei from DMSO:GBL solutions template the growth of larger, rounded grains. Any residual DMSO would introduce an impurity trap site, enabling

trap-assisted recombination losses under illumination. However, X-ray diffraction spectra (XRD, Figure 2.3) of DMSO:GBL-spun perovskites indicate high crystallite purity, suggesting that DMSO evaporates completely during annealing.[38] DMF, however, is not observed to coordinate as strongly with lead halides,[13] yielding smaller nuclei which promote the formation of a small-grained perovskite film. AFM micrographs (Figure 2.2) show that small-grained films exhibit reduced roughness, which would be advantageous for layered devices.

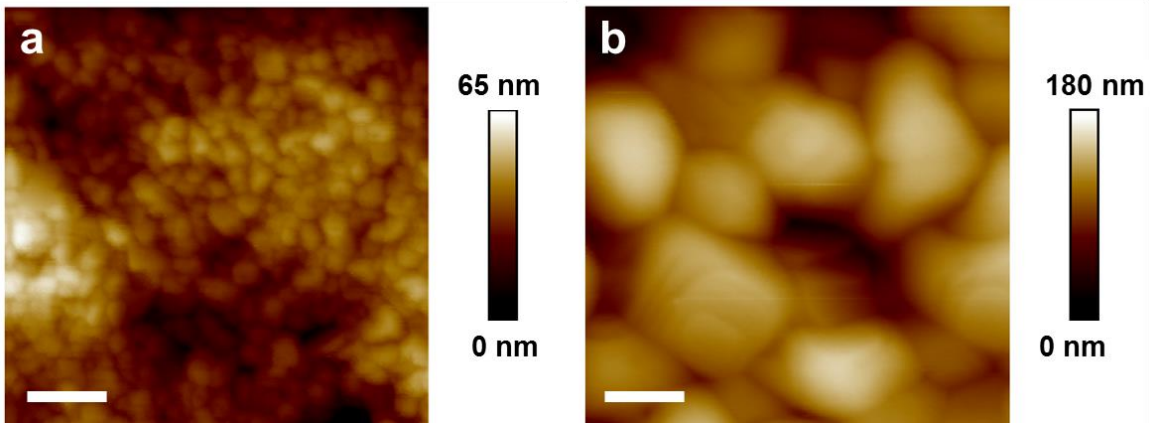

Figure 2.2: AFM micrograph of (a) perovskite film spin-coated from DMF reveals smaller grains with lower roughness than (b) perovskite film spin-coated from a 3:7 v/v solution of DMSO:GBL exhibit rounded grains with higher roughness. Scale bars are 200 nm.

To compare the quality of perovskite crystal domains, X-ray diffraction (XRD) spectra were collected for $CH_3NH_3PbI_3$ produced from DMF and from DMSO:GBL as displayed in Figure 2.3. The labeled peaks represent diffraction planes in $CH_3NH_3PbI_3$ perovskite as reported in Oku,[39] and the absence of other peaks indicate a high film purity. Notably, the diffraction counts for DMF perovskites are lower, even if peak area is integrated. This could signify the presence of an amorphous connective phase, as discussed further in Chapter 3. The broader XRD peaks of DMF-spun perovskites indicate smaller grains, and the average crystallite diameter *d* was

estimated using the Scherrer equation with K = 1, λ = 0.154 nm, and FWHM representing the XRD peak width at half maximum: $d = \frac{K\lambda}{FWHM * \cos\theta}$

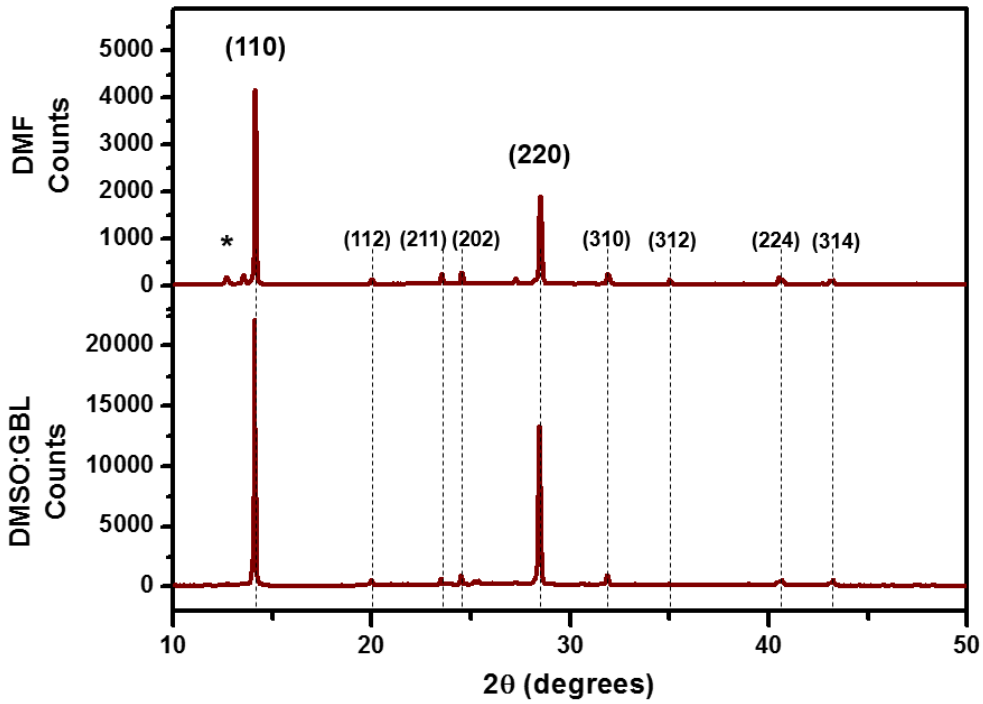

Figure 2.3: Full XRD spectra of $CH_3NH_3PbI_3$ perovskite films from DMF and DMSO:GBL, with peaks of interest labeled with corresponding crystallographic planes in tetragonal $CH_3NH_3PbI_3$ perovskite. The peak labeled with (*) represents a minority phase of PbI_2, likely due to surface oxidation in air during spectral acquisition.

When bromide is incorporated in the synthesis of $CH_3NH_3Pb(I_{1-x}Br_x)_3$ perovskites, the grain-scale morphology is unaffected for either grain structure. The precursor is mixed with a ratio of PbI_2, CH_3NH_3I, or CH_3NH_3Br for the desired composition x in $CH_3NH_3Pb(I_{1-x}Br_x)_3$, and the resultant crystal compositions revealed by EDS are practically exact. The nearly identical SEM images across bromide compositions in Figure 2.4 provide visual evidence that the grain structure is adequately controlled for optoelectronic experiments. This consistency is expected because all crystals below x ~ 0.4 are most thermodynamically stable in the tetragonal geometry at room temperature.[26] Any subtle differences in focus or contrast likely stem from inconsistent machine settings (highly dependent on substrate conductivity, beam settings, and chamber vacuum). Within these grains, the introduction of competing halogen ions creates compositional variations that give rise to interesting optical phenomena, which will be discussed in Chapter 3.

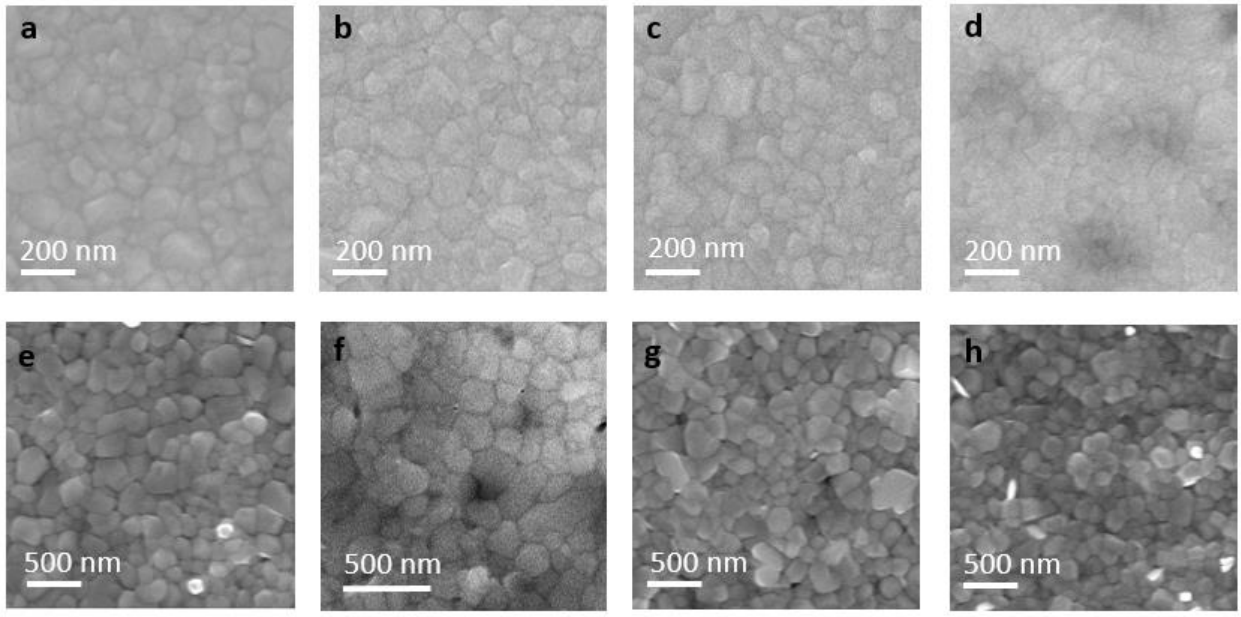

Figure 2.4: SEM micrographs of $CH_3NH_3Pb(I_{1-x}Br_x)_3$ show that grain morphology is consistent across Br compositions. Images (a)-(d) are top-views of perovskite films deposited from DMF with x=0, 0.1, 0.2, and 0.33, and (e)-(h) are films deposited from DMSO:GBL with x=0, 0.1, 0.2, and 0.33, respectively.

Indirect evidence exists for an amorphous connective phase at grain edges, assisted by the slower kinetics of bromide incorporation into perovskite. Recent literature has implicated a chloride-rich connective phase between grains in $CH_3NH_3Pb(I_{1-x}Cl_x)_3$ perovskites for superior device performance and sustained carrier lifetimes compared to $CH_3NH_3PbI_3$.[35] The lower grain boundary contrast in SEM coupled with longer carrier lifetimes hint that bromide could preferentially occupy lattice edges to a similar effect. Furthermore, the (110) peak shift in XRD toward the cubic structure ($2\theta = 15°$) with increasing bromide concentration could evidence this amorphous connective phase. This observed shift is generally attributed to a crystallographic transition from tetragonal to cubic lattice as bromide replaces iodide, as the larger iodide atoms cause an offset of the PbX_6 octahedra in perovskite.[38] Added strain from the abundance of edges and interfaces with an amorphous phase likely exacerbates that effect, explaining the additional shift away from the unstrained cubic lattice ($2\theta = 15°$).[39]

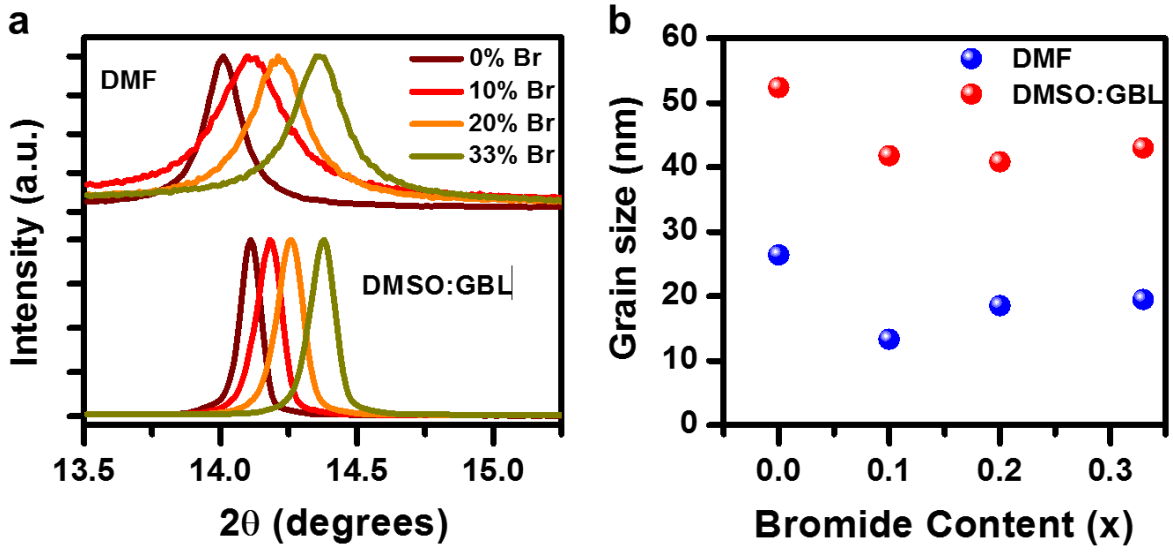

Figure 2.5: (a) XRD peaks from the (110) plane of DMF-spun (top) and DMSO:GBL-spun (bottom) perovskite films indicate a shift toward more cubic crystallinity ($2\theta = 15°$) with increased Br content and with larger grains. (b) The grain size calculated from the Scherrer equation represents the average diameter of single crystals.

Table 2.6: Average grain diameters from AFM image analysis and from the Scherrer equation. Error from image analysis is the standard deviation.

Spin solvent	Method	x = 0	x = 0.1	x = 0.2	x = 0.33
DMF	Image	55 ± 10 nm	55 ± 10 nm	50 ± 8 nm	50 ± 10 nm
	Scherrer	26.4 nm	13.3 nm	18.5 nm	19.5 nm
DMSO:GBL	Image	200 ± 40 nm	200 ± 35 nm	210 ± 40 nm	180 ± 50 nm
	Scherrer	52.3 nm	41.7 nm	40.8 nm	43.0 nm

The grain size calculated using XRD peak widths in Scherrer's equation indicates that DMF-spun grains are 2-3 times smaller than DMSO:GBL-spun grains, and all Scherrer diameters are significantly smaller than those estimated from AFM image analysis (see Table 2.6). Since AFM micrographs did not reveal any observed differences in morphology between perovskite films of varying Br content, we estimated a grain diameter of 50 ± 12 nm for the DMF-spun films for all Br-doped samples and 200 ± 50 nm for films obtained with DMSO:GBL, though crystallite size is much smaller in both cases. The Scherrer equation underestimates the grain sizes due to the polycrystalline nature of the perovskite films, and this effect is exacerbated in Br-doped perovskites due to the local variability of Br ion lattice positions.[40] This compositional inhomogeneity likely stems from imperfect mixing of the precursor and from nucleation of I-rich and Br-rich domains present before spin coating. The recent revelation that iodide and bromide can diffuse through perovskite crystals even in the absence of solvent complicates characterization, as these iodide-rich and bromide-rich domains could be highly mobile.[40] The clear peaks in XRD indicate that any such domains comprise a tiny fraction of the bulk grains, but the ones that are present will play a major role in carrier recombination.

For future incorporation into devices, it is essential that perovskite active layers have maximized physical and energetic alignment with the electron- and hole-selective contacts. A complication to early device tests was the porosity inherent to antisolvent crystallized films; these

perovskite layers made poor contact with the electron-collecting TiO_2 substrate, and the devices short-circuited from the deposition of spiro-OMeTAD hole transport material in these pores. To eliminate this porosity, perovskite films were annealed in an atmosphere of DMF, which enabled the crystals to slowly settle and reform in contact with the base layer, as shown in Figure 2.7. The solvent anneal incurred an additional 1 h at 100 °C underneath a 20 mL petri dish with 50 µL of additional DMF. The resulting film had a higher roughness due to uneven grain stacking, but the gains in intergranular and substrate contact show promise in future device production.

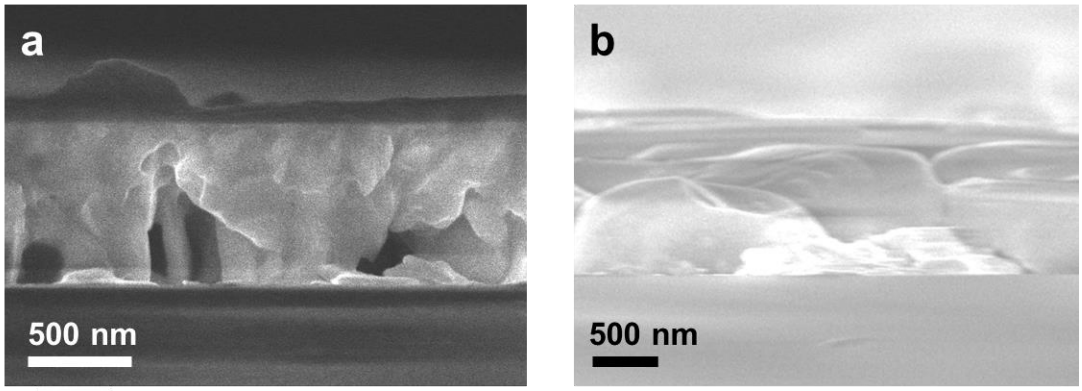

Figure 2.7: Cross-sectional SEM of DMF-spun perovskite films (a) annealed in nitrogen atmosphere versus (b) annealed in a DMF-rich atmosphere. The DMF vapor allows the perovskite crystals to melt and reform with lower porosity and improved substrate contact.

The thickness of planar perovskite films can be tuned by varying the molarity of the precursor and the spin speed of deposition. As precursor salts are diluted with additional solvent, nucleation lessens and resultant grains are smaller (this is counterintuitive to many nucleation arguments, but the antisolvent treatment causes more individual grains to crash out in the absence of nuclei). The reduction of available perovskite also causes the films to be thinner. Likewise, increasing the spin speed also generates thinner films, though this trend is somewhat limited by the antisolvent treatment. The antisolvent treatment only works as intended in a narrow range of

spin speeds (approximately 1000-3000 rpm); the separation between toluene and precursor phases is compromised at low spin speeds, whereas massive polycrystalline formations have already deposited at high spin speeds. Full results of these optimizations are shown in Figure 2.8.

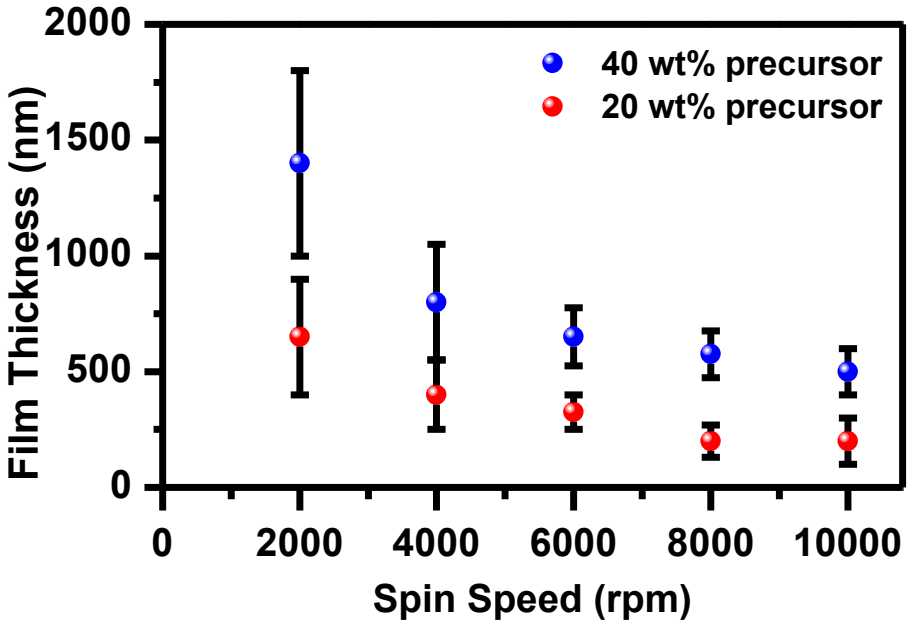

Figure 2.8: Thickness of perovskite films spin-coated from DMF depends on precursor concentration and spin speed.

Finally, the annealing temperature plays a role in resulting morphology. Both DMF and DMSO:GBL solvents are said to fully evaporate from perovskite during a 1 h anneal at 100 °C, which was confirmed by XRD. However, multiple studies of temperature effects on film crystallization noted that $CH_3NH_3PbI_3$ undergoes a phase transition from tetragonal to cubic around 140 °C and posited that this reversible phase change encourages defect removal. As shown in Figure 2.9, annealing at 150 °C for 30 min provoked a grain-scale rearrangement, forming definite tetragonal crystals after cooling. The roughness of these films was significantly higher, prompting the adoption of the 100 °C covered solvent anneal for optoelectronic studies. Besides,

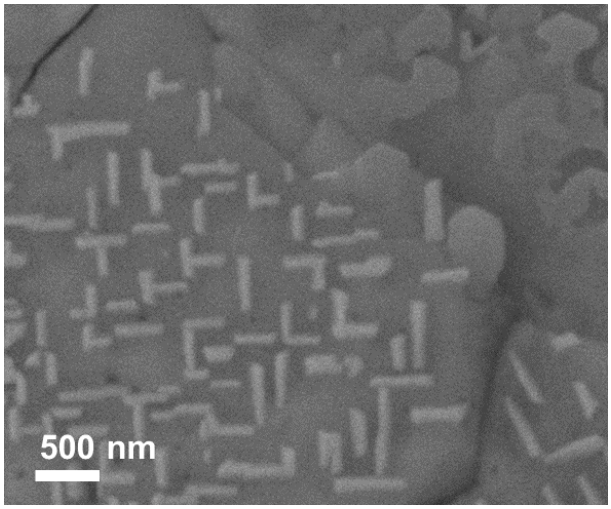

Figure 2.9: SEM micrograph of $CH_3NH_3PbI_3$ perovskite film from DMF annealed at 150 °C shows rearrangement into angular tetragonal crystals.

the mobility of iodide and bromide is predicted to increase at higher temperatures, and the high temperature anneal may result in more rearrangement into iodide-rich and bromide-rich phases. While other groups have published efficient planar devices using both low- and high-temperature annealing processes, the temperature effect on the optoelectronic performance of our $CH_3NH_3Pb(I_{1-x}Br_x)_3$ films is unclear and merits further investigation.

It is well established that smooth films with few grain boundaries are desirable for planar $CH_3NH_3PbI_3$ solar cells. After a discussion of synthetic techniques for $CH_3NH_3PbI_3$-type planar films, tunability of film thickness and grain structure is demonstrated. Chapter three will deeply examine two of these morphologies, ~500 nm thick films from 40 wt% precursor in DMF versus from 40 wt% precursor in 3:7 v/v DMSO:GBL, inferring further detail about the crystalline substructure of mixed halide perovskites from steady-state and time-resolved photoluminescence experiments.

B. *Mesoporous Perovskites: Control of Optical Density and Bromide Concentration*

Mesoporous titania scaffolds provide an avenue for repeatable, two-step synthesis of high-performance $CH_3NH_3PbI_3$-like perovskite films. In the first step of device synthesis, a thin blocking layer of compact TiO_2 is deposited on FTO-glass substrates to prevent hole injection directly from perovskite into the FTO electrode. The compact TiO_2 deposition step is preserved in our synthesis of freestanding films on glass as it promotes adhesion of TiO_2 nanoparticles in the formation of the mesoporous scaffold. Next, a suspension of ~20 nm TiO_2 nanocrystals in 2:1 v/v α-terpineol:ethanol is spin-coated onto the substrate and subsequently fired at 500 °C to fuse the nanocrystals into a rigid mesoporous matrix. The thickness of this mesoporous scaffold can be readily tuned by varying the spin rate and concentration of nanoparticles in suspension (Figure 2.10). Typical devices require a m-TiO_2 layer that is ~300-500 nm thick: when coated with perovskite, this is the minimum thickness for near-complete (99%) light absorption in the visible range.

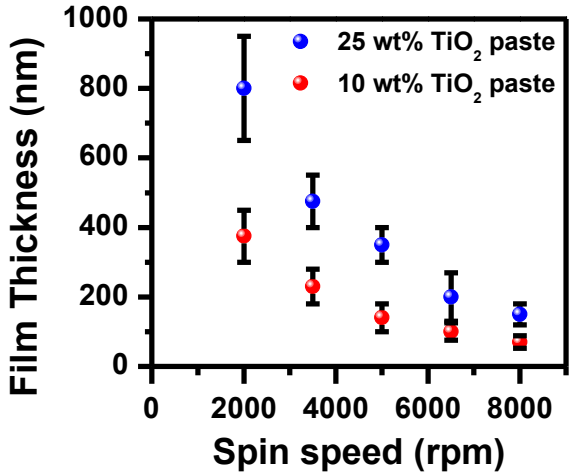

Figure 2.10: Thickness of mesoporous TiO_2 is controlled by TiO_2 nanoparticle concentration and spin speed.

The perovskite is deposited in two steps. A solution of PbI_2 ($PbCl_2$ is often used in other studies in the literature) is pipetted onto the substrate, and several seconds are allowed for the lead halide to seep into the pores before spinning. As the spin rate increases, the PbI_2 inside the pores crystallizes in increased surface contact with the m-TiO_2 support, and excess PbI_2 on top of the m-TiO_2 film is mostly centrifuged off. A relatively high spin rate of 6000 rpm is used with the goal of minimizing the perovskite capping layer that forms on top of the mesoporous scaffold. This capping layer can be detrimental to solar device performance by increasing roughness and inhibiting hole transport out of the active layer. For the second step, the PbI_2-coated mesoporous substrate is immersed in a 0.8 M solution of CH_3NH_3I in isopropanol. The substrate turns from yellow to dark gray within seconds, signaling that CH_3NH_3I successfully incorporated into the PbI_2 crystals to form $CH_3NH_3PbI_3$. Prolonging the soak for a minute or more allows for complete reaction of CH_3NH_3I with PbI_2; while the diffusivity of CH_3NH_3I in PbI_2 and $CH_3NH_3PbI_3$ is high, the nanoscale nature of the porous matrix ensures that the crystallization reaction is mass transfer limited. The isopropanol solvent does not interact with PbI_2 or perovskite (Pb-O coordination is weak for the secondary alcohol, so solubility is minimal), which is essential for constraining the perovskite crystal growth. The perovskite is annealed for 30 min at 70 °C. In full devices, a hole transport material of p-doped spiro-OMeTAD (2,2′,7,7′-tetrakis[*N*,*N*-di-*p*-methoxyphenyl-amine]9,9′-spirobifluorene with added bis(trifluoromethane)sulfonimide lithium and cobalt salts) is subsequently spin-coated, and a gold counterelectrode is thermally evaporated to complete the device. Devices of this basic design have achieved power conversion efficiencies of up to 8% in our lab, compared to about 14% for highly performing devices in literature.[41-43]

For optoelectronic characterization, it is beneficial for perovskite films to have a reduced optical density so changes in light absorption can be effectively quantified. A 100 mg/mL solution

of PbI_2 is spin-coated onto a 200 nm thick mesoporous titania scaffold at 6000 rpm, resulting in the correct amount of PbI_2 deposition for full perovskite coverage. Then the substrate is immersed in a saturated CH_3NH_3I solution in isopropanol. The grain size of the perovskite depends on both the amount of available PbI_2 and the concentration of the CH_3NH_3I soak solution. High availability of both species promotes perovskite nucleation, so the minimum grain size of 100-200 nm is achieved using maximum concentration of CH_3NH_3I and coverage of PbI_2. The crystallite dimensions are limited inside the mesoporous layer, so this grain size refers to the perovskite capping layer as viewed with SEM (Figure 2.11). A small grain size is preferred to reduce the film thickness and limit the roughness of the capping layer. Photophysics of the capping and mesoporous perovskite layers should be identical, but the charge injection into TiO_2 is a function of geometry so the capping layer is engineered to be thin compared to the mesoporous scaffold.

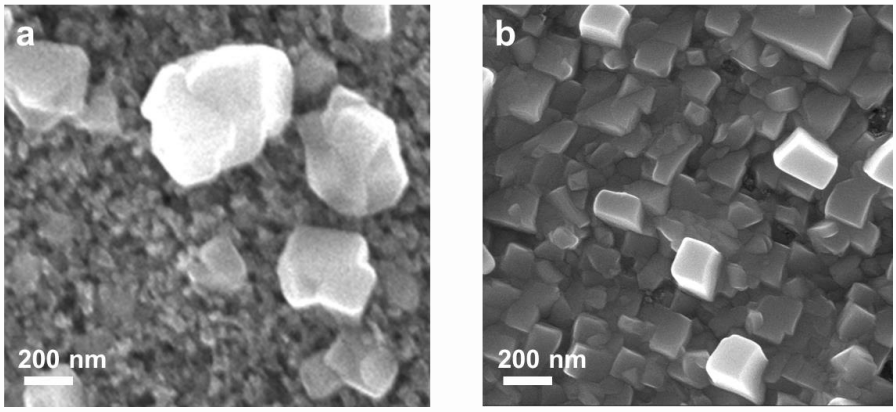

Figure 2.11: Scanning electron micrographs of mesoporous TiO_2-supported $CH_3NH_3PbI_3$ perovskites produced with (a) 0.8 M versus (b) saturated 1.2 M CH_3NH_3I soak solutions. A saturated soak solution reduces the grain size and promotes full coverage of the titania support.

To produce $CH_3NH_3Pb(I_{1-x}Br_x)_3$, mesoporous TiO_2 substrates are coated similarly with PbI_2 then immersed in an appropriate mixture of CH_3NH_3I and CH_3NH_3Br. Control of the resulting perovskite composition is complicated by the competing kinetics of each of these ions. By starting with stoichiometric mixtures of CH_3NH_3I/CH_3NH_3Br and $PbI_2/PbBr_2$, it was revealed that the

incorporation of iodide occurs at a slightly faster rate than bromide. However, bromide-rich perovskites are known to be thermodynamically favored.[44] The mechanism of crystallization from mixed CH_3NH_3I/CH_3NH_3Br soak solutions therefore has two steps. First, iodide is incorporated into the lattice at a faster rate than bromide by the following reactions:

$$PbI_2 + I^- + CH_3NH_3^+ \rightarrow CH_3NH_3PbI_3$$

$$PbI_2 + Br^- + CH_3NH_3^+ \rightarrow CH_3NH_3PbI_2Br$$

As time progresses, the crystal composition moves toward (and eventually past) the solution concentration of iodide and bromide until it reaches an equilibrium in which the crystal is more bromide-rich than the solution. When bromide displaces iodide, it reduces the diffusivity of ions through the lattice, especially limiting the diffusion of the larger iodide ions. Bromide is incorporated by the following mechanism in the presence of excess $CH_3NH_3^+$:

$$CH_3NH_3Pb(I_{1-x}Br_x)_3 + Br^- \rightarrow CH_3NH_3Pb(I_{1-x'}Br_{x'})_3 + I^-$$

A 1 min soak time was chosen to limit compositional variability introduced by the second reaction. The final composition was verified using EDS, and the soak concentrations used for optoelectronic experiments are shown as stars in Figure 2.12. The final concentration falls between the traces of kinetically-controlled crystallization (lower line, assuming equal rates of iodide and bromide incorporation) and equilibrium crystallization (upper line, assuming crystal composition matches

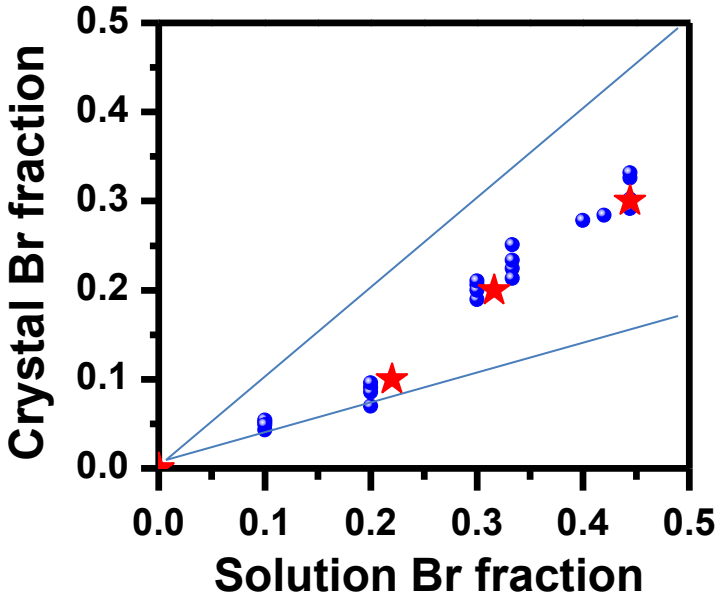

Figure 2.12: Mixed halide perovskite composition as a function of soak solution concentration. The lower line represents the composition expected from kinetic incorporation of halides, and the upper line represents compositional equilibrium with the solution. The starred compositions were used for optoelectronic characterization.

solution halide ratio). For low bromide concentrations, the effect of the substitution reaction is muted. As bromide concentration is increased, the crystal composition deviates from the solution composition at an increasingly monotonic rate as predicted by equilibrium thermodynamics. Notably, the kinetic and thermodynamic traces are not absolute limits, as faster iodide incorporation kinetics and enhanced bromide thermodynamic stability permit data points outside the pictured range.

Because the bromide composition was more difficult to control for the mesoporous geometry than for the planar geometry, the ratio of halides in the soak solution was chosen by interpolation of the data in Figure 2.12. This correlation is only valid for the reaction of 200 nm titania-supported PbI_2 films immersed in a saturated solution of CH_3NH_3I/CH_3NH_3Br in isopropanol for 1 min. The final perovskite composition can be modified if the concentration of

methylammonium halide is decreased, the soak time extended, or the PbI_2 thickness varied. Further study on varying PbI_2 substrate thicknesses/geometries is warranted to determine detailed kinetics of templated perovskite formation. For the purpose of the optoelectronic study of absorption dynamics, steady compositions within 2% of the target were the primary goal of the optimization. The crystallography, a purely composition-dependent property, is expected to be similar for mesoporous and planar mixed halide perovskites. However, the templated nature of the two-step perovskite synthesis should reduce compositional variation within the film, especially for longer soak times. The TAS experiments performed on these mesoporous samples are discussed in chapter four, illuminating excited-state dynamics introduced by bromide doping and the presence of a mesoporous electron acceptor.

CHAPTER 3

Charge Transport and Recombination in Planar $CH_3NH_3Pb(I_{1-x}Br_x)_3$ Perovskites

Grain structure and lattice uniformity both play a major role in dictating charge transport in perovskite films, wherein well-connected grains with defect-free crystallinity are generally desired for high-performance devices.[45-48] This chapter builds upon the previous chapter's morphological discussions of planar $CH_3NH_3Pb(I_{1-x}Br_x)_3$ perovskite films by incorporating optoelectronic observations, including absorbance, steady-state and time-resolved photoluminescence. To explain an anomaly in photoluminescence behavior, a morphology-dependent recombination mechanism is proposed, and SEM and STEM-EDS evidence for low-bandgap recombination centers is presented.

A major advantage of doping $CH_3NH_3PbI_3$ with bromide is the ability to tune the bandgap of the absorptive layer of the solar cells. With increasing bromide concentration, excitons are more tightly bound by the lead and bromide ionic nuclei, leading to a bandgap increase that is advantageous for solar cells with higher operating voltages.[22, 49] Absorbance spectra (Figure 3.1) of $CH_3NH_3Pb(I_{1-x}Br_x)_3$ films show that the absorption band edge shifts from around 770 nm for pure $CH_3NH_3PbI_3$ films into the visible range for $CH_3NH_3PbI_2Br$. The corresponding increase in absorptive bandgap, i.e. the photon energy needed to excite an electron-hole pair in the perovskite, is approximately linear with increasing Br content (Figure 3.3), as shown previously in the literature.[22, 26, 50] Notably, the band edge blueshifts similarly for perovskite films from DMF and from DMSO:GBL. Differences in sub-bandgap extinction, namely any absorbance at wavelengths longer than the band edge, signify reflection or refraction from surface roughness. The DMF-spun

perovskite film absorbance gives a clearer view of band edge shifting with increasing bromide content, but the rougher DMSO:GBL-spun films show nearly identical band edge, indicating that perovskite with the same bulk composition was produced irrespective of solvent.

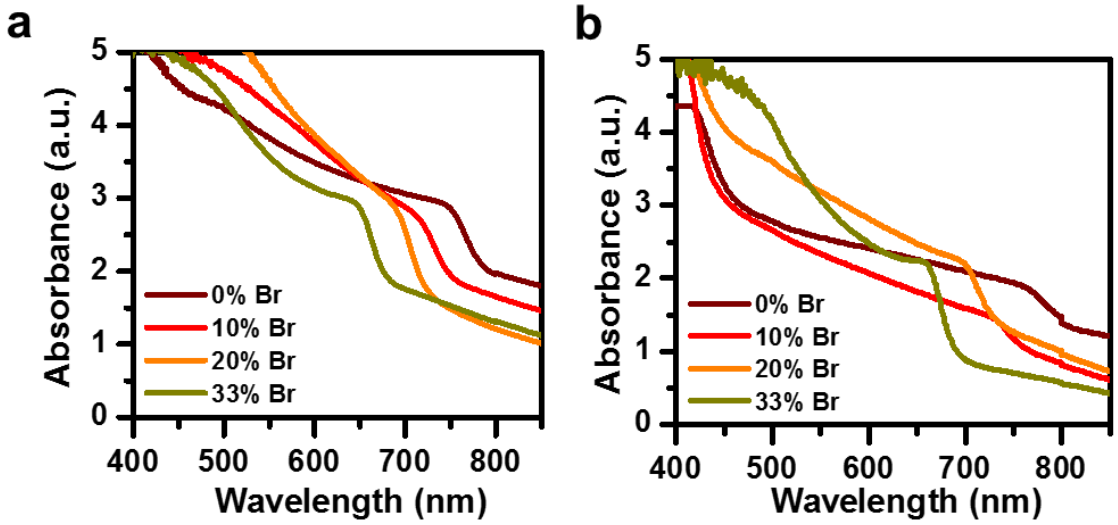

Figure 3.1: Absorbance spectra of (a) DMF-spun $CH_3NH_3Pb(I_{1-x}Br_x)_3$ films and (b) DMSO-spun $CH_3NH_3Pb(I_{1-x}Br_x)_3$ films show a band edge blueshift with increasing bromide composition, corresponding to an increase in bulk bandgap.

However, the fluorescence peak shifts with increasing Br composition (Figure 3.2) are considerably less pronounced compared to absorbance, an anomalous effect previously attributed to bandgap variation within the perovskite film.[25, 26] In mixed-ion perovskites, the photons emitted from the recombination of electron-hole pairs are released at a lower energy than would be expected from the absorption band edge. Park et al.[26] suggested that $CH_3NH_3PbI_3$ nuclei within the crystalline films of mixed halide perovskites act as recombination centers of lower bandgap energy, which would predict that the fluorescence emission for all bromide concentrations would remain near 1.6 eV. However, the fluorescence peaks still shift for both film structures, indicating that grain morphology and bromide content both contribute to the minimum conduction band energy. The discrepancy between the absorption and fluorescence bandgaps can be attributed to

the kinetics of recombination in mixed halide perovskites, as electron-hole pairs are most likely to undergo recombination in regions of the film where the bandgap is the narrowest.[27]

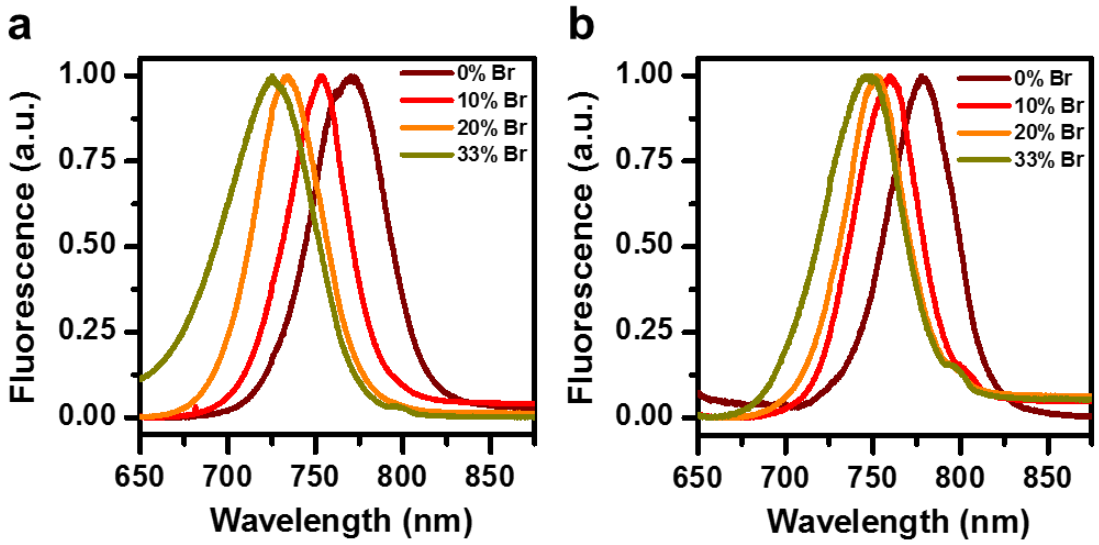

Figure 3.2: Fluorescence peaks of (a) DMF-spun $CH_3NH_3Pb(I_{1-x}Br_x)_3$ films show a more pronounced blueshift with increased bromide content than (b) DMSO-spun $CH_3NH_3Pb(I_{1-x}Br_x)_3$ perovskites.

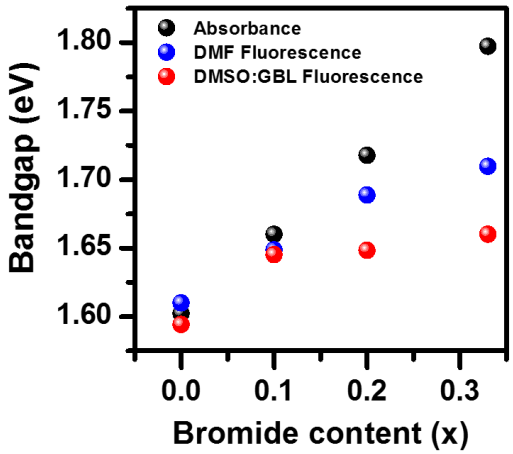

Figure 3.3: Bandgaps calculated from absorbance band edges and fluorescence peaks show a marked difference in recombination energetics for DMF-spun and DMSO:GBL-spun films.

While the absorbance profiles of DMF-spun and DMSO:GBL-spun perovskites are nearly identical, photoluminescence behavior (Figure 3.2) shows a strong dependence on grain morphology. The polycrystalline DMF-spun perovskites exhibit a more pronounced blueshift in their fluorescence peaks for increasing bromide content than did the large-grained films deposited from DMSO:GBL, indicating that the minimum bandgap in $CH_3NH_3Pb(I_{1-x}Br_x)_3$ films from DMF is closer to the mixed ion bandgap than in equivalent films from DMSO:GBL (Figure 3.3). As $CH_3NH_3PbI_3$ nuclei are inherently present in the precursor before spin-coating, we attribute the discrepancy in peak shift to the size difference of iodide-rich domains, as schematically represented in Figure 3.4. In this depiction, the DMF-spun perovskites contain smaller iodide-rich recombination cores with a wider fluorescence bandgap, whereas DMSO:GBL-spun perovskites exhibit larger recombination cores with a diffuse edge and a narrower bandgap. This structural difference results from DMSO complexation with PbI_2 in the precursor: we predict that though larger $CH_3NH_3PbI_3$ nuclei are expected, diffusion of bromide ions into the nuclei during film crystallization creates an energy gradient in the conduction and valence band levels that encourages carrier recombination. The carrier lifetimes as determined from time-resolved photoluminescence (discussed at the end of this chapter) are significantly longer for DMF-produced perovskite films, supporting the proposed nucleus-driven recombination model. It is worth noting that pure $CH_3NH_3PbI_3$ and $CH_3NH_3PbBr_3$ crystals are undetectable in absorbance or XRD spectra, so pre-formed $CH_3NH_3PbI_3$ nuclei comprise only a small fraction of the film.

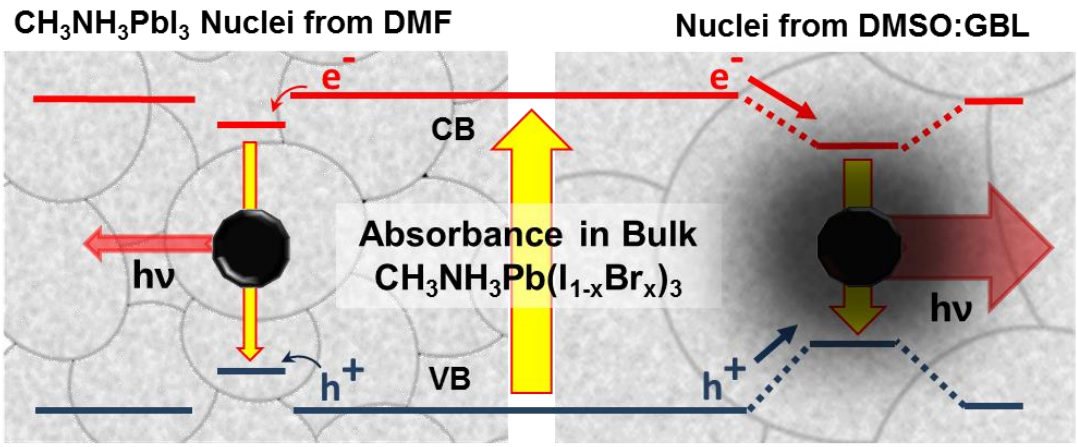

Figure 3.4: Schematic depicting the proposed nuclei-driven recombination mechanism. DMF-spun crystals contain smaller discrete iodide-rich nuclei, which limit recombination. DMSO complexation forms larger nuclei while allowing a bromide concentration gradient as DMSO is evolved, and this gradient favors carrier trapping and subsequent recombination.

The slight but continuous increase in fluorescence bandgap energy implies that recombination at $CH_3NH_3PbI_3$ centers is likely influenced by the surrounding bromide content. The relevant distance where recombination occurs is within the Bohr exciton radius (2.8 nm in $CH_3NH_3PbI_3$),[51] and the relative presence of bromide ions within this radius is expected to contribute to the blueshifting of photoluminescence peaks. Because of their larger size and internal bromide content, low-bandgap nuclei in DMSO:GBL-produced $CH_3NH_3Pb(I_{1-x}Br_x)_3$ films are less influenced by bulk bromide composition, and the fluorescence peak positions more closely resemble the bandgap of $CH_3NH_3PbI_3$. DMF-produced films, on the other hand, are more influenced by bromide composition, as the emitted photon is expected to carry the energy of the bandgap averaged over the Bohr exciton radius. Because hole density is limited in the $CH_3NH_3PbI_3$ nuclei due to a very stable valence band,[52] recombination is favored at the interface between $CH_3NH_3PbI_3$ nuclei and the bulk perovskite. For recombination to occur, three particles need to interact; an electron and hole need to come in proximity to one another as well as couple

with a phonon to dissipate the excess energy. This three-body interaction is more common in the larger DMSO:GBL grains because thermalization is expected to occur on a longer timescale; thus, recombination in DMSO:GBL-spun films occurs more quickly than recombination in DMF-spun films.

While the presence of these nuclei can be interpreted from spectral analysis alone, visual evidence of these nuclei certainly enhances the understanding of recombination dynamics in mixed halide perovskites. STEM-EDS maps of $CH_3NH_3Pb(I_{0.9}Br_{0.1})_3$ from DMF-spun perovskites (Figure 3.5a) reveal compositional variation and provide visual evidence of $CH_3NH_3PbI_3$ nucleation. Although color differences in the bulk are likely a result of signal noise, the bright green area in the lower part of the perovskite grain pictured in Figure 3.5a represents an iodide-rich core of ~5 nm diameter. Bromide-rich spots toward the right edge of the pictured grain also identify compositional variation; whether these indicate $CH_3NH_3PbBr_3$ nuclei or simply edge regions of disproportionately high Br content is inconclusive. However, no compositional

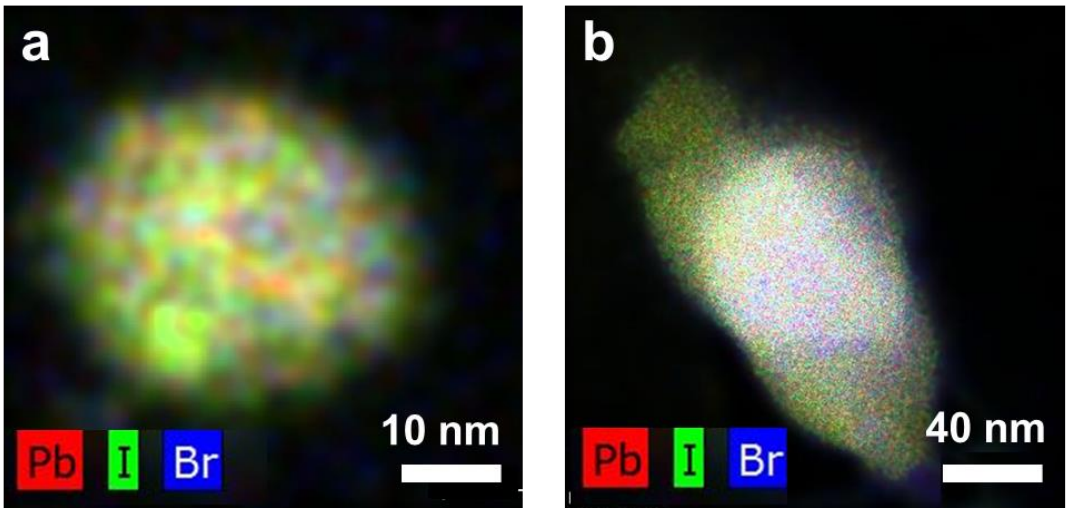

Figure 3.5: STEM-EDS maps of (a) DMF-spun and (b) DMSO:GBL-spun $CH_3NH_3Pb(I_{0.9}Br_{0.1})_3$ grains. Compositional variation including an iodide-rich subcrystal is evident in the smaller DMF-spun grains but may also exist in the thicker DMSO:GBL-spun perovskite.

variation is visible in the DMSO:GBL-produced perovskite (Figure 3.5b), apart from a blue glow around the edges that may or may not represent a bromide-rich passivating layer. This is not alarming because the thickness of the pictured grain (100-200 nm) would obscure subtle compositional variations on the predicted sub-10 nm scale. Because STEM-EDS is a transmission technique, EDS intensities are integrated along the transmitted beam with no vertical differentiation. A drawback to STEM-EDS is that the electron beam can severely damage perovskite crystals; methylammonium is vaporized along with some halogens within minutes (at the standard beam settings of 200 kV accelerating voltage, 200 nA probe current), limiting the EDS map integration time. Nevertheless, any compositional variation leads to bandgap variation, where regions of lowest bandgap are the dominant sites for recombination.

SEM micrographs of $CH_3NH_3Pb(I_{1-x}Br_x)_3$ films from DMF (Figure 3.6) provide further evidence of the presence of localized recombination centers. In SEM, the image is generated from reflected electrons, and contrast is generated by surface features such as grain edges. The bright spots, shown in low contrast, represent electron scattering from defect sites of finite size. Their presence in only Br-doped films supports our hypothesis that these spots represent the low bandgap cores rather than some other type of defect. Moreover, these bright spots gradually disappear with prolonged beam exposure, indicating that they are not a product of beam damage. Notably, SEM did not reveal distinct low-bandgap nuclei in grains from DMSO:GBL, which lends credence to the hypothesis that nuclei from DMSO:GBL precursor solutions can incorporate Br ions and compositionally blend with the bulk as depicted in Figure 3.4.

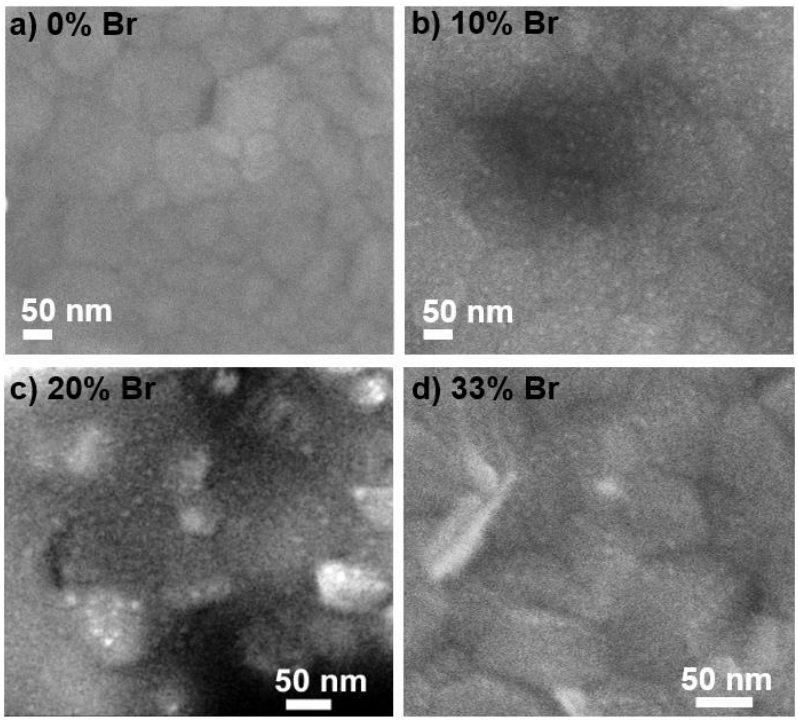

Figure 3.6: High-resolution SEM micrographs of (a) $CH_3NH_3PbI_3$, (b) $CH_3NH_3Pb(I_{0.9}Br_{0.1})_3$ (c) $CH_3NH_3Pb(I_{0.8}Br_{0.2})_3$ and (d) $CH_3NH_3PbI_2Br$ films from DMF. Imaging over a low contrast range, we identify bright spots in Br-doped films from DMF, which we attribute to electron scattering from low-bandgap $CH_3NH_3PbI_3$ nuclei.

While ss-PL provided a qualitative look at energy band variations with Br dopant and grain sizes, tr-PL provides a complementary quantitative evaluation of charge transport, illustrating the lifetime of individual carriers between excitation and relaxation events on a sub-nanosecond time scale. Initial electronic excitation of the perovskite with a 400 nm laser pulse generates electron-hole pairs which separate and propagate through the perovskite lattice. When an electron-hole pair recombines, a photon is emitted, and the time between excitation and emission is recorded as the lifespan of the photogenerated carriers. For this experiment, the excitation laser and single photon avalanche diode collector were focused on a highly luminescent area of the crystalline film with a spot size of ~1 μm. A number of studies have correlated the lifetimes of methylammonium lead

trihalide perovskites from multiple exponential fits with various carrier decay processes, including first-order, second-order, and Auger recombination.[53-57] The tr-PL decay transients (Figure 3.7) of the DMF-spun and DMSO:GBL-spun perovskite films demonstrate that carrier lifetimes increase with Br content (Figure 3.8). Lifetimes were obtained by fitting the tr-PL transients with the following biexponential model:

$$PL = A_1 e^{-t/\tau_1} + A_2 e^{-t/\tau_2}$$

$$\tau = \tau_{avg} = \frac{A_1\tau_1 + A_2\tau_2}{A_1 + A_2}$$

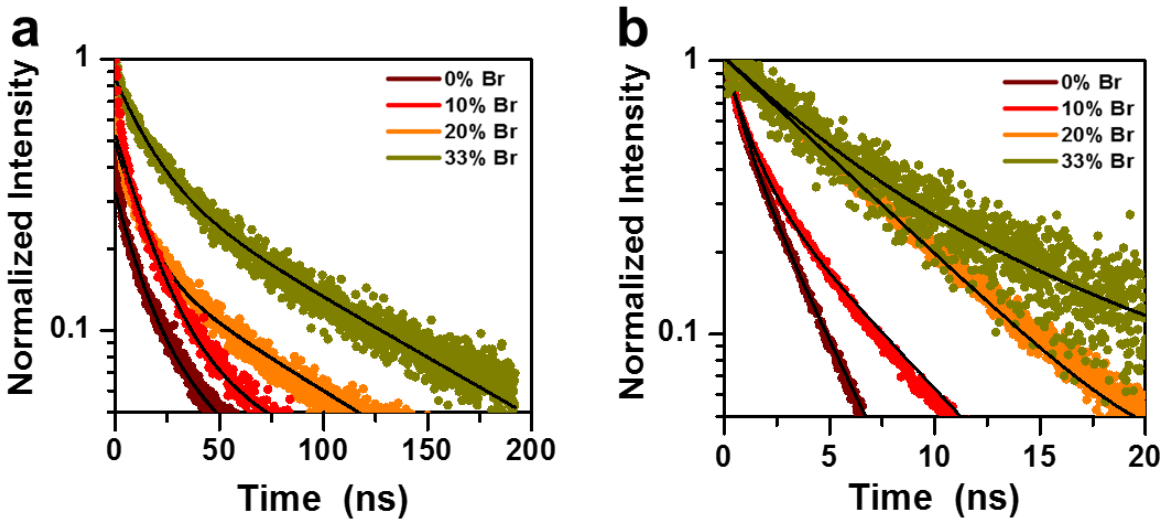

Figure 3.7: Time-resolved photoluminescence decay transients of (a) DMF-produced and (b) DMSO:GBL-produced $CH_3NH_3Pb(I_{1-x}Br_x)_3$ films.

Although larger grains are generally expected to display longer carrier lifetimes, the smaller grained DMF-spun perovskite films show an order-of-magnitude increase in carrier lifetimes compared to their DMSO:GBL-spun counterparts. This observed difference in lifetime

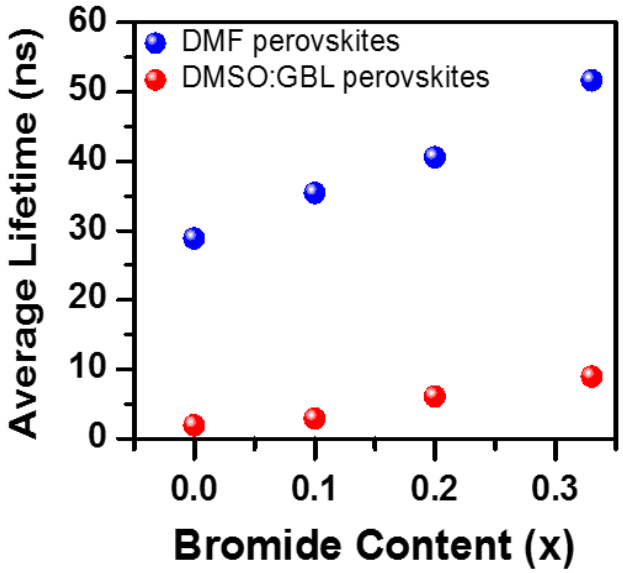

Figure 3.8: Combined tr-PL lifetimes of $CH_3NH_3Pb(I_{1-x}Br_x)_3$ films increase with bromide content, and are an order of magnitude longer for films produced from DMF than from DMSO:GBL.

at all Br concentrations is explained by the combined effect of smaller recombination nuclei and increased grain connectivity in the DMF-spun films. The shorter lifetimes of DMSO:GBL-spun perovskite films signify higher rates of carrier trapping, which are mainly attributable to larger bromide-deficient nuclei as depicted in Figure 3.4. Bromide-deficient areas of the crystal would have a higher probability of trapping conduction band electrons, which subsequently relax on the time scale of picoseconds.[58] Thus, the lifetimes observed in our tr-PL measurements on the order of nanoseconds capture the carrier diffusion in the bulk prior to sub-nanosecond relaxation. The increase in carrier lifetime with increasing bromide content supports previous results that bromide doping can improve carrier transport in organolead halide perovskites.[26, 40] In uniform bulk films, this can be correlated to the decreasing angle of the tetragonal lattice offset, reported to be 15° for $CH_3NH_3PbI_3$ but ~0° for $CH_3NH_3PbBr_3$,[59] which promotes directional charge transport and extends the carrier lifetime. However, compositional variations are unavoidable in reality, so this decreased lattice offset only applies to bulk carrier diffusion prior to encountering a recombination

nucleus. The progressive loss of this offset in the bulk is indicated by the (110) peak shift toward 15° in XRD (Figure 2.7).

Table 3.9 lists all time constants and amplitudes for the tr-PL fits; notably, carrier lifetimes differ more drastically between grain structures than for progressive Br doping. While there are no discernable trends in time constants τ_1 and τ_2 nor in weighted amplitudes A_1 and A_2, the relative timescales of these constants fall within a reasonable range for each crystal type. τ_1 is often assigned to trap-assisted recombination, as the one-body relaxation can occur on a timescale of a few nanoseconds. τ_2 is often ascribed to geminate recombination within the bulk phase, as the two-body collision of electron and hole occurs at a reduced rate. These second-order recombination lifetimes are generally 10-100 ns for bulk films but can extend to several microseconds for perovskite single crystals.[60, 61]

Table 3.9: Complete lifetime data from biexponential fits of tr-PL decays of $CH_3NH_3Pb(I_{1-x}Br_x)_3$ films.

Spin solvent	**Parameter**	**Bromine Content**			
		x = 0	**x = 0.1**	**x = 0.2**	**x = 0.33**
DMF	τ_1	11.53 ns	14.70 ns	11.06 ns	16.03 ns
	τ_2	67.16 ns	116.1 ns	91.66 ns	98.52 ns
	A_1	0.6962	0.8045	0.6414	0.5637
	A_2	0.3362	0.2112	0.4072	0.4878
	$\boldsymbol{\tau_{avg}}$	**29 ns**	**35 ns**	**41 ns**	**52 ns**
DMSO:GBL	τ_1	0.7813 ns	1.127 ns	6.036 ns	4.834 ns
	τ_2	2.682 ns	5.328 ns	n/A	18.81 ns
	A_1	0.4657	0.5935	1.0	0.7281
	A_2	0.6085	0.4103	n/A	0.3043
	$\boldsymbol{\tau_{avg}}$	**1.9 ns**	**2.8 ns**	**6.0 ns**	**8.9 ns**

These results suggest that both grain morphology, driven by the precursor solvent, and bromide content control carrier recombination in mixed-halide perovskite films. The anomaly in photoluminescence bandgaps, noticed by several groups but never fully explained, hints that iodide-rich nuclei exist and assume different forms in DMF-produced and DMSO:GBL-produced films. Further evidence from electron microscopy shows that small perovskite subcrystals are abundant in DMF-spun films, though compositional variations in DMSO:GBL-spun perovskites are obscured by the large grain size and are expected to be even more pronounced. In the design of future solar devices based on mixed halide perovskites, more emphasis should be placed on maximizing compositional uniformity, and a morphological understanding can aid in these endeavors.

CHAPTER 4

Absorption Dynamics in Mesoporous $CH_3NH_3Pb(I_{1-x}Br_x)_3$ Perovskites

Film microstructure and lattice composition also play a role in absorption dynamics. Mesoporous $CH_3NH_3Pb(I_{1-x}Br_x)_3$ perovskite films, whose synthesis was discussed in section B of chapter two, were probed with transient absorption spectroscopy to find trends in excited-state behavior for various bromide compositions within the $CH_3NH_3PbI_3$-like regime. While excited-state decay lifetimes show no dependence on bromide content, the bleach formation and stabilization becomes faster with increased bromide doping. This signifies that bromide introduction promotes faster carrier thermalization (by increasing the thermal conductivity at the lattice scale), though carrier injection and trap-assisted recombination remain constant across the range of bromide compositions.

Transient absorption spectroscopy is a powerful tool for probing short-lived excited state dynamics in photochemically interesting materials. In perovskites, TAS examines the relaxation from a state of conduction band saturation back to the ground state on a picosecond timescale. Information about the radiative and non-radiative recombination, charge injection, and carrier thermalization can all be extracted from changes in absorbance. TAS is a pump-probe spectroscopy: the excited state is pumped full of charge carriers using high-intensity laser illumination. For most of our measurements, the sample is pumped with approximately 0.25 mW at 1 kHz repetition (0.25 mJ or $5 * 10^{11}$ photons per pulse) at 400 nm wavelength, well above the bandgap of $CH_3NH_3Pb(I_{1-x}Br_x)_3$. Changes in absorbance of a white light probe are monitored at all wavelengths with a monochromator/photodetector setup. Sub-picosecond resolution in time

points is obtained by moving the sample on a motorized linear stage to vary the optical path length (and thus the collection delay) between the sample and the photodetector. Raw TAS data is generally plotted as evolutionary spectra of change in absorbance at several time points, normalized by subtracting steady-state absorbance from transient spectra.

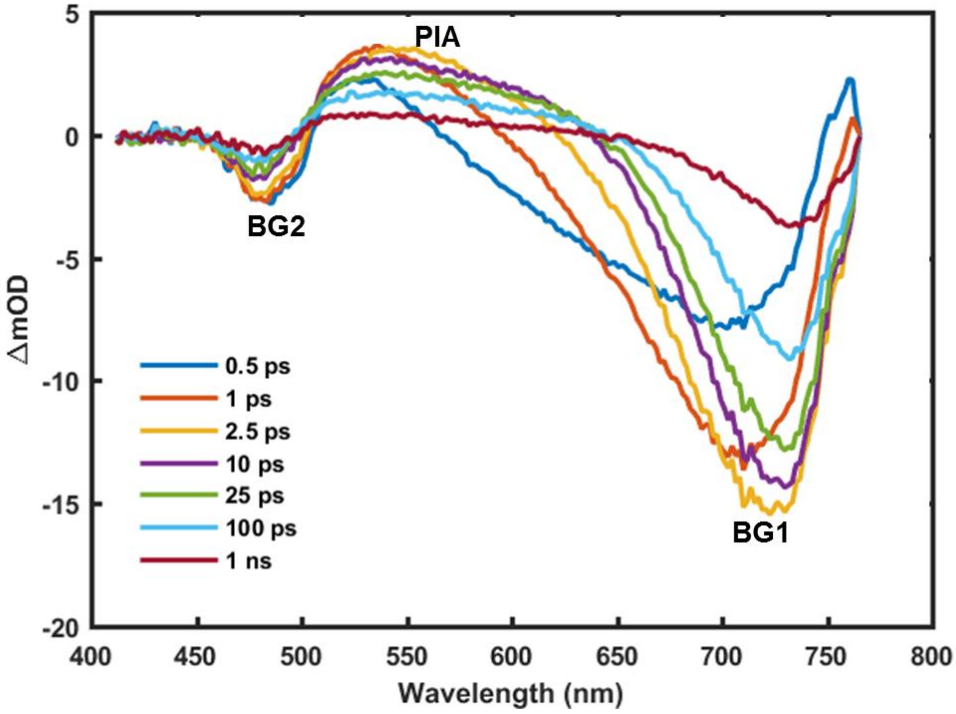

Figure 4.1: Evolutionary TAS spectra of $CH_3NH_3PbI_3$ perovskite supported on a 200 nm-thick scaffold of mesoporous TiO_2, displaying the time evolution of bleach modes and photoinduced absorption of $CH_3NH_3PbI_3$-type perovskites after the pump laser pulse.

Typical TAS spectra for $CH_3NH_3PbI_3$-type perovskites have three major features: two photobleach peaks corresponding to valence band depletion and conduction band saturation, and a broadband photoinduced absorption (PIA) in between, as labeled in Figure 4.1. The main bleach labeled BG1 corresponds to electron depletion from the HOMO level of the perovskite, and the secondary bleach labeled BG2 reflects depletion from a deeper valence state. Most studies to date

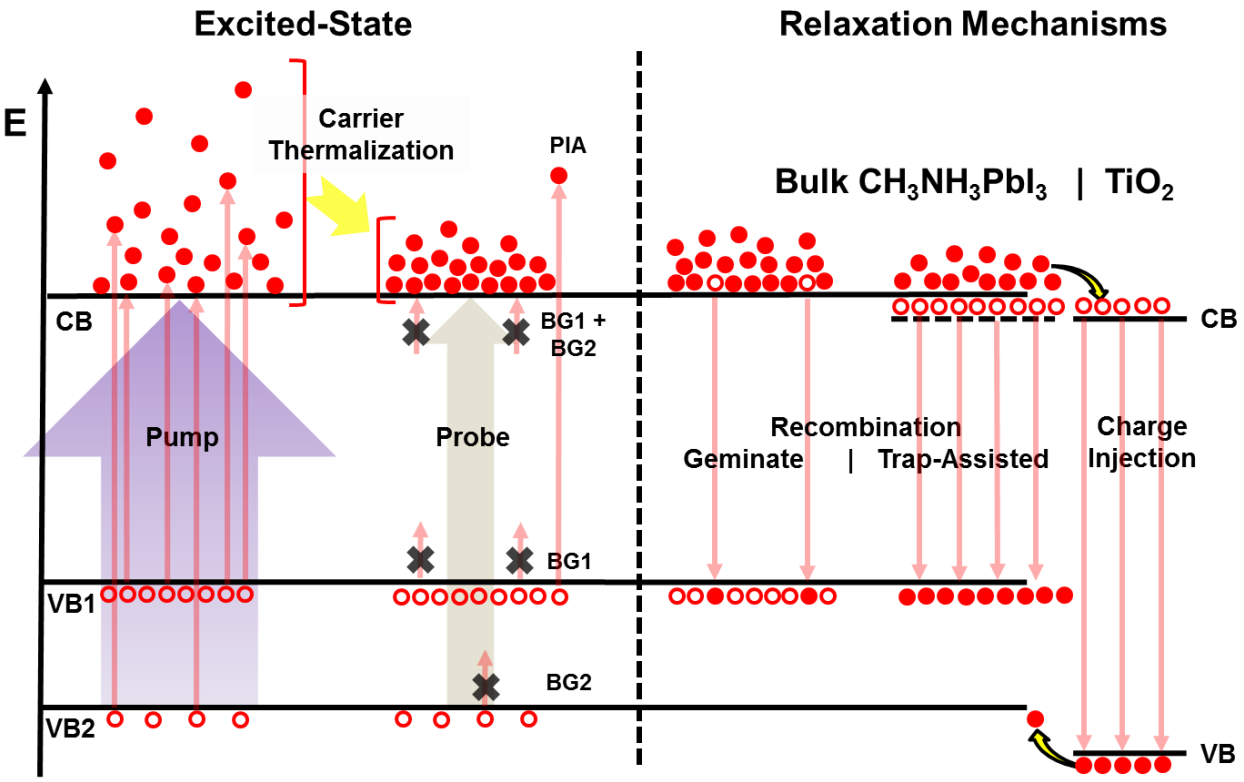

Figure 4.2: Energy diagram of various excited-state decay processes identifiable by TAS. Electrons are pumped into the conduction band then thermalize to a quasi-equilibrium distribution, where the optical transitions of a white-light probe are either bleached or enhanced depending on photon energy. The excited state decays through subsequent recombination (bulk or trap-assisted) to repopulate VB1 and through charge injection to TiO_2 to repopulate VB2.

have focused on the shape and decay kinetics of the BG1 bleach feature, which occurs 0.05-0.1 eV above the perovskite bandgap.[9, 61-69] The shape of this bleach feature mirrors the excited-state population, and its change over time echoes the quasi-equilibrium cooling of carriers.[66] In perovskites and similar semiconductor materials, a bleach occurs when an overpopulation of excited states or an under availability of valence electrons prevents interband transitions that would occur under normal operating conditions. At early times, the broadband bleach indicates that conduction electrons exist in substantial populations well above the bandgap. The bleach area shifts to longer wavelengths as carriers dissipate energy to the lattice, and the bleach peak position stabilizes just above the bandgap after a few picoseconds. Finally, the bleach peak decays as

carriers recombine or inject into TiO_2 and the valence band is repopulated, retaining its general shape. Since the white light probe is of low intensity and causes negligible depletion, the bleach disappears completely at long times as the perovskite absorbance returns to its ground-state spectrum.

The spectral shape of bleach features can be explained by quantum mechanics. Electrons populate available states in a Fermi-Dirac distribution, so the transition from full occupation above the bandgap to no occupation below the bandgap is not abrupt. Moreover, the conduction and valence bands are parabolic in k-space,[70] which prevents the maximum carrier population from existing precisely at the bandgap. Rather, the maximum depletion occurs about 0.05-0.10 eV above the bandgap, corresponding to the maximum photobleach intensity. This shift is referred to as the Burstein-Moss effect, where high electron populations near the conduction band minimum (and hole populations near the valence band maximum) cause the bandgap to appear wider.[63] The BG2 bleach shape is similarly governed by Fermi-Dirac statistics and parabolic bands, albeit for a wider bandgap that represents excitation from a deeper valence band.[64, 65] However, both bleach features are distorted by the broad photoinduced absorption band which extends from the onset of BG2 out into the infrared. This feature is commonly approximated as parabolic, but also depends on sample considerations such as light absorption and charge injection.[71] As such, it is imprudent to oversimplify the integrated peak area as a carrier energy distribution; this distribution can only be inferred from the deconvolution of bleaching effects from photoinduced absorption and temporal chirp effects.

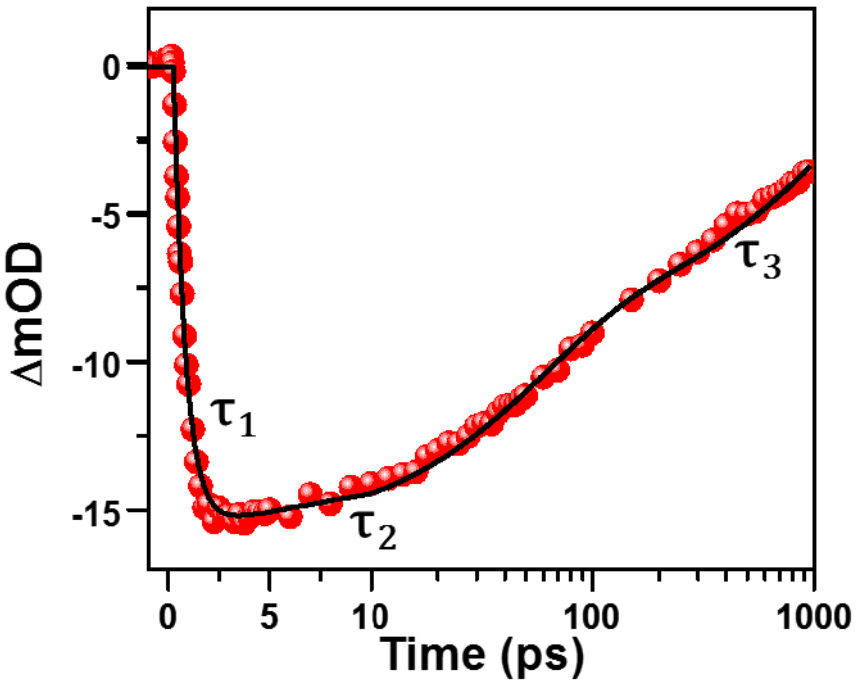

Figure 4.3: Dynamics of the BG1 bleach in mesoporous $CH_3NH_3PbI_3$ perovskite fit with a triexponential function – one exponent representing bleach formation and two exponents representing the mechanisms of bleach decay.

The BG1 bleach kinetics (Figure 4.3) can be resolved by fitting the intensity averaged around the wavelength of the absolute minimum change in optical density to the following triexponential function:

$$\Delta OD = A_1 e^{-t/\tau_1} - A_2 e^{-t/\tau_2} - A_3 e^{-t/\tau_3}$$

The three lifetimes obtained represent the timescales of three different relaxation mechanisms. Several studies have employed a biexponential fit to the bleach decay, and their reported lifetimes correspond well to our second and third lifetimes on the order of 50 ps and 1 ns, respectively. The shorter exponential decay is a subject of ongoing debate, but the leading assertion is that it models trap filling at defect sites and grain boundaries.[62, 66] In fact, pioneering studies using TAS as a

microscopy tool identified that "dark grains" of low photoluminescence yield exhibited a characteristic decay on the order of 30-100 ns.[68, 69] It logically follows that these trap states at grain edges sequester conduction band electrons on a short time scale for nonradiative recombination. The longer exponent is widely attributed to charge injection, the main avenue for carrier relaxation in mesoporous perovskite films.[62, 72-74] The process of carrier diffusion and injection occurs in about a nanosecond timescale, which is barely resolvable in our recorded domain of 1 ns delay. As discussed in chapter three, radiative recombination in the perovskite occurs on the timescale of several nanoseconds; we expect that a third decay exponent would be relevant for extended time domains, and that nanosecond recombination could slightly skew our calculated charge injection lifetimes.

Because our experimental setup can achieve 50 fs resolution, we see a distinct exponential curvature within the sub-picosecond bleach formation. This first lifetime on the order of 500 fs is attributed to carrier thermalization in the direct aftermath of the laser pulse. When an electron absorbs a photon above the bandgap, it gains all of the photon's energy to reach temperatures of several thousand Kelvin.[66] The hot electron subsequently couples with a phonon to dissipate excess heat, relaxing to the thermal equilibrium for carriers in the range of 300-700 K. Analogously, a sub-picosecond lifetime has been assigned to exciton dissociation, as bound excitons would not inhibit interband transitions.[67] Note that the bleach formation lifetimes are not decoupled from Gaussian signal appearance, meaning that thermalization/exciton dissociation lifetimes could be shorter than the exponential fits would indicate.

The main objective of the TAS experiment was to examine the differences in TAS spectra for mesoporous $CH_3NH_3Pb(I_{1-x}Br_x)_3$ with varying bromide composition. Evolutionary spectra (Figure 4.5) show similarly shaped traces for compositions between 0 and 30% bromide, an

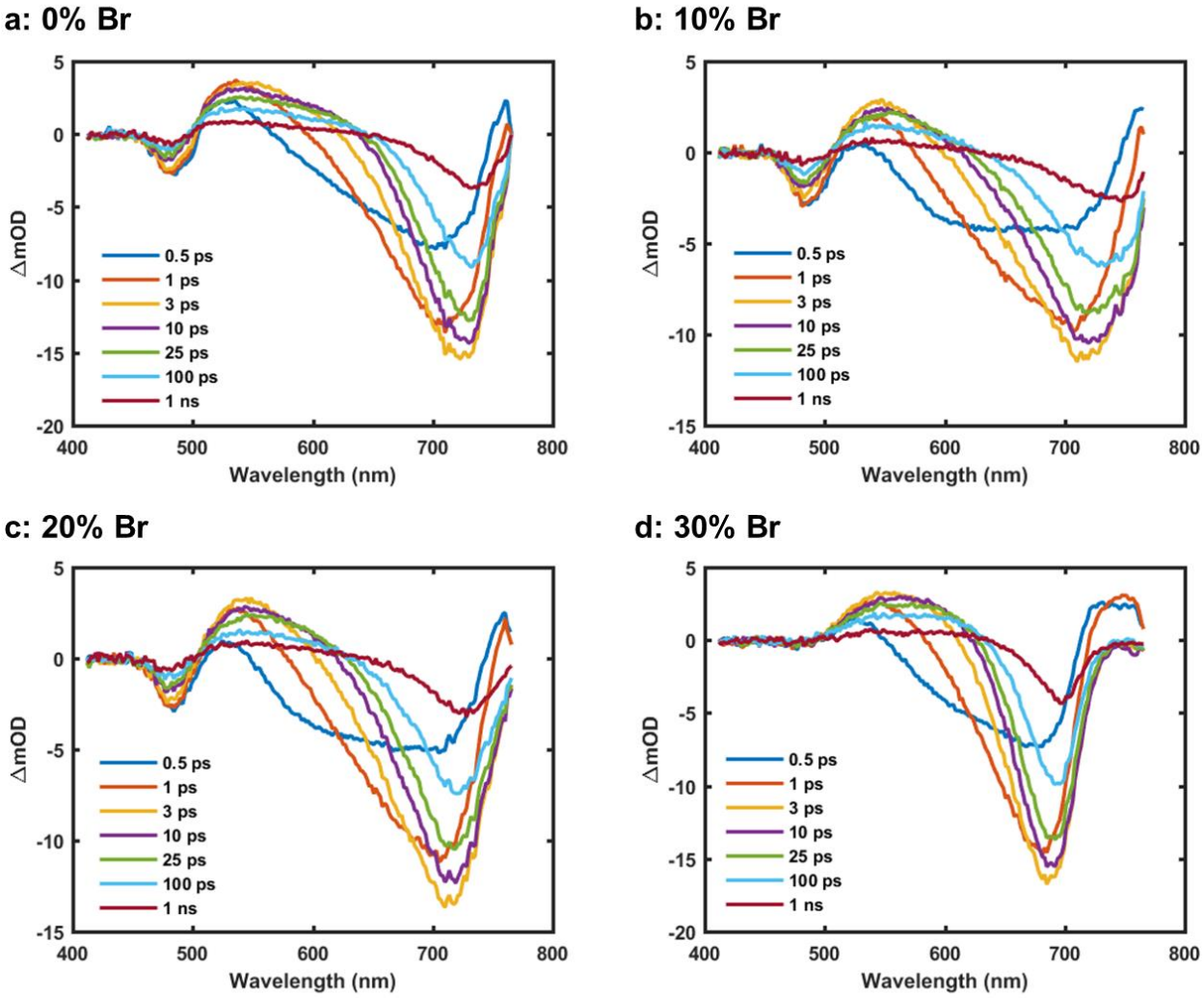

Figure 4.4: Evolutionary spectra of mesoporous $CH_3NH_3Pb(I_{1-x}Br_x)_3$ with (a) x=0, (b) x=0.1, (c) x=0.2, and (d) x=0.3 show similar excited state dynamics with a clear redshift in the major BG1 bleach feature.

expected result for perovskites of the same crystalline regime. The only major visible difference is the shift in BG1 wavelength that follows the blueshift in absorption band edge. Comparing the decay kinetics at the peak BG1 bleach for each bromide concentration (Figure 4.5), both τ_2 and τ_3 are approximately the same for all compositions. This parity suggests that carrier trapping and charge injection are not predominantly affected by bromide content. Given that carrier drift

velocity is relatively constant for all tetragonal $CH_3NH_3PbI_3$-type perovskites,[26] lifetimes for these relaxation events are more strongly a function of geometry than local crystallinity.

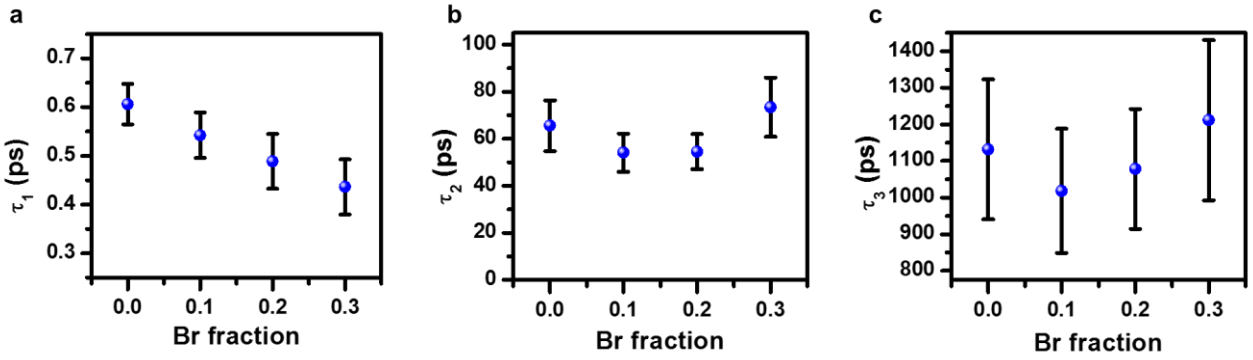

Figure 4.5: Fitted lifetimes for the (a) rapid formation of the BG1 bleach, (b) short-lived decay due to carrier trapping, and (c) BG1 bleach decay due to charge injection in m-TiO_2 supported $CH_3NH_3Pb(I_{1-x}Br_x)_3$ perovskites. While bleach decay lifetimes τ_2 and τ_3 remain relatively constant, the bleach formation lifetime τ_1 decreases with bromide content as phonon transport improves.

Bromide introduction to the perovskite lattice clearly influences the bleach formation kinetics, however. The thermalization lifetime of $CH_3NH_3PbI_3$ is twice as long as that of $CH_3NH_3Pb(I_{0.7}Br_{0.3})_3$, indicating that phonon coupling is twice as efficient in the bromide-doped perovskite. A hot phonon bottleneck has previously been identified in $CH_3NH_3PbI_3$ perovskites, as electron thermalization is limited by phonon coupling to hot electrons for large hot carrier populations.[66] Lifetimes of unrestricted thermalization are theorized to peak at 100 fs,[65] but we measure thermalization lifetimes up to six times longer in iodide-rich perovskites. In the same way that bromide ions promote carrier transport by reducing the tetragonal lattice offset, phonon propagation should also benefit from a more cubic crystal structure. Future TAS experiments with

varying laser fluences will further elucidate the dependence of the hot phonon bottleneck on bromide content.

The other spectral features also provide motivation for future experiments. The BG2 bleach, whose kinetics are plotted in Figure 4.6, represents the depletion of deeper valence states, which are only refilled by charge injection.[64] Increasing the bromide content should gradually disrupt the band alignment between perovskite and TiO_2, which would lead to decreased charge injection. The disappearance of the BG2 bleach can identify decreased charge injection and possible emergence of alternative mechanism for interband relaxation. However, our experiments have yielded inconsistent trends in BG2/BG1 ratio, as BG2 bleach intensity is expected to directly depend on interfacial contact area between perovskite and m-TiO_2, a parameter that is prone to some variability. The kinetics of the BG2 bleach decay can again be modeled with a triexponential

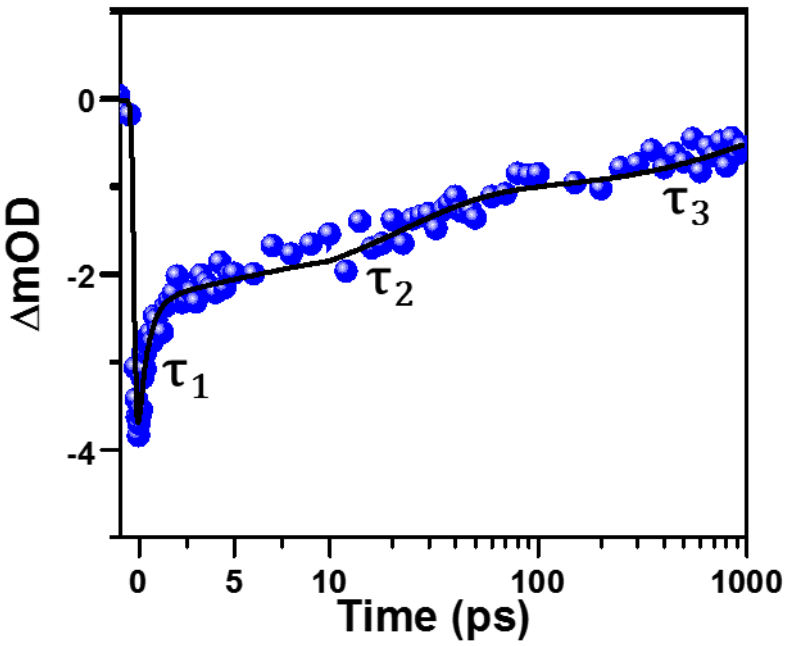

Figure 4.6: Dynamics of the BG2 bleach in mesoporous $CH_3NH_3PbI_3$ perovskite fit with a triexponential decay function.

function, although all three lifetimes are decays. There is no exponential delay in bleach formation, demonstrating that the decay arises solely from valence band depletion. The mechanisms behind the three lifetimes are undocumented, as it has been noted that the timescales of these exponents matches only with the lifetimes of the PIA decay and not at all with BG1 kinetics.[64] Likewise, the PIA transient has three distinct exponential lifetimes, as pictured in Figure 4.7. The bleach at early times originates from the broadband bleach, and this lifetime parallels the non-equilibrium thermalization lifetime for BG1 bleach formation. Then, the decay in stimulated absorption represents the refilling of the uppermost valence band by recombination (τ_2) and charge injection (τ_3). The PIA lifetimes are within a similar range to those of BG1, indicating that they depend on both the conduction and valence populations.

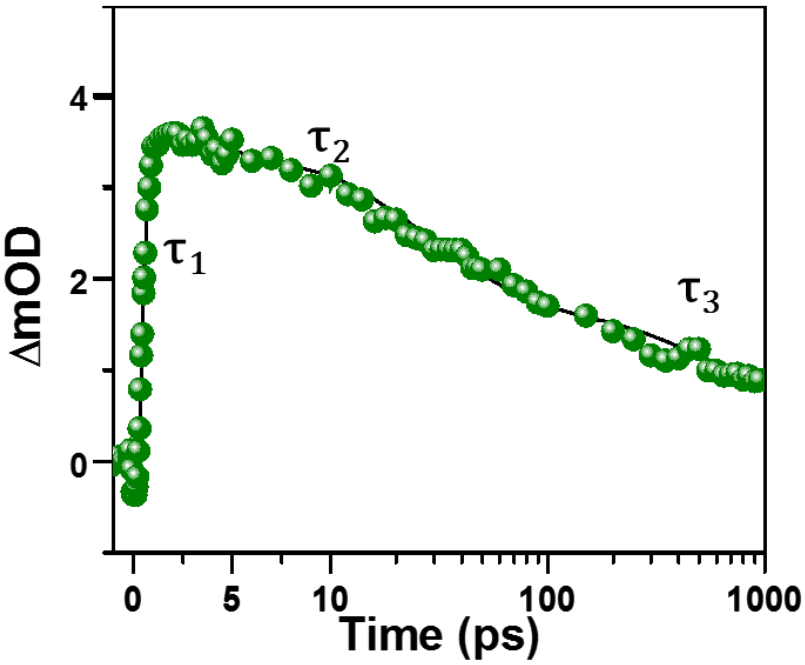

Figure 4.7: Dynamics of the photoinduced absorption feature in mesoporous $CH_3NH_3PbI_3$ perovskite fit with a triexponential function.

Transient absorption spectroscopy, while an increasingly popular tool for characterizing hybrid perovskites, still has many gaps in knowledge. A major source of confusion in the field comes from competing terminology: many researchers attribute bleach features to conventional band energetics (citing the Burstein-Moss effect, the Stark effect, and valence depletion) whereas others exclusively refer to these observations as a product of excitonic effects. Major advances in the understanding of hybrid perovskite excited-state dynamics will only occur when the effects of bandgap energy and exciton binding energy are decoupled. However, the observation of accelerated bleach formation in bromide-containing perovskites provides valuable insight into their improved thermal dissipation, which could improve photostability in future devices. Future collaborative work between our lab and the Center for Nanophase Materials Science at Oak Ridge National Laboratory will aim to further the understanding of $CH_3NH_3Pb(I_{1-x}Br_x)_3$ perovskites, focusing on carrier population dynamics and charge injection.

CHAPTER 5

Conclusion

Mixed halide hybrid perovskites of the formula $CH_3NH_3Pb(I_{1-x}Br_x)_3$ with interesting optoelectronic properties that can vary widely with bromide composition and grain morphology. Planar perovskite films were spin-coated from DMF-based and DMSO:GBL-based precursor solutions, resulting in two starkly different grain structures. These films were probed with steady-state and time-resolved photoluminescence spectroscopies, and carrier lifetimes were maximized in DMF-spun films of the highest bromide content. A discrepancy in photoluminescence peak shifts alluded to strong bandgap variation within the mixed halide crystals, and a recombination mechanism based on precursor nucleation is proposed. A manuscript detailing this work, titled "Interplay of Structural and Compositional Effects on Carrier Recombination in Mixed-Halide Perovskites," is currently under review for the journal *RSC Advances*. $CH_3NH_3Pb(I_{1-x}Br_x)_3$ perovskites were also synthesized via a two-step deposition for mesoporous TiO_2-supported architectures, and soak conditions for controlling the bromide composition of low optical density (~200 nm thick) perovskites were optimized. These films were probed with TAS, which revealed that carrier thermalization lifetimes decreased with bromide content while charge injection and recombination processes were unaffected by bromide substitution. In this ongoing project, we hope to obtain a clearer picture of quasi-equilibrium carrier cooling and charge injection in future experiments.

Beyond publishing, the impact of this work can be realized in the application of its concepts to future design of optoelectronic devices. While $CH_3NH_3PbI_3$ is shaping up into the basis for

imminent commercialization of perovskite solar cells, bromide ions can readily be substituted into existing synthetic routines without disrupting the tetragonal crystal structure. An understanding of charge transport and recombination is valuable for optimization in this application. $CH_3NH_3Pb(I_{1-x}Br_x)_3$ perovskites are perhaps more valuable in the continual search for tunable emitters for use in colored and white-light LEDs. By varying the bromide content, the bandgap can be tuned to result in emission wavelengths between 530 nm and 770 nm. Recognition of the impact of compositional variation, especially due to iodide-rich subcrystals from precursor nucleation, on fluorescence wavelength can guide the manufacturing process to minimize such variations. If these nuclei cannot be fully eliminated, introduction of oxidative traps to iodide-rich recombination centers could quench the unwanted near-infrared fluorescence from these sites by enabling nonradiative recombination. Moreover, the knowledge that bromide in mixed halide perovskites encourages heat transfer at the nanoscale is also beneficial for emissive applications, as these devices are prone to damage by buildup of electrons or waste heat. Finally, the data presented may help clarify a major gap in the understanding of mixed halide perovskite photophysics: the unknown role of mobile ions in engendering the unique optoelectronic properties. While Hoke et al. proposed that iodide and bromide can diffuse freely and form segregated domains under light illumination,[40] this work rebuts that intrinsic halide compositional variation from precursor nucleation influences the apparent bandgap, as this effect does not diminish as would be expected from a freely diffusing system. Further, the movement of halide ions in the excited state would likely differ from the ground state, a phenomenon which could affect the subtle dynamics of TAS. There are many potential benefits to bromide substitution in $CH_3NH_3PbI_3$-type perovskites, which can only be fully realized through thorough photophysical characterization.

REFERENCES

1. A. Kojima, K. Teshima, Y. Shirai and T. Miyasaka, *J. Am. Chem. Soc.*, 2009, **131**, 6050-6051.
2. W. S. Yang, J. H. Noh, N. J. Jeon, Y. C. Kim, S. Ryu, J. Seo and S. I. Seok, *Science*, 2015, **348**, 1234-1237.
3. M. M. Lee, J. Teuscher, T. Miyasaka, T. N. Murakami and H. J. Snaith, *Science*, 2012, **338**, 643-647.
4. H.-S. Kim, C.-R. Lee, J.-H. Im, K.-B. Lee, T. Moehl, A. Marchioro, S.-J. Moon, R. Humphry-Baker, J.-H. Yum, J. E. Moser, M. Graetzel and N.-G. Park, *Sci. Rep.*, 2012, **2**.
5. M. A. Green, A. Ho-Baillie and H. J. Snaith, *Nat. Photonics*, 2014, **8**, 506-514.
6. G. E. Eperon, V. M. Burlakov, P. Docampo, A. Goriely and H. J. Snaith, *Adv. Funct. Mater.*, 2014, **24**, 151-157.
7. T. Dittrich, C. Awino, P. Prajongtat, B. Rech and M. C. Lux-Steiner, *J. Phys. Chem. C*, 2015, **119**, 23968-23972.
8. K. Galkowski, A. Mitioglu, A. Miyata, P. Plochocka, O. Portugall, G. E. Eperon, J. T.-W. Wang, T. Stergiopoulos, S. D. Stranks, H. J. Snaith and R. J. Nicholas, *Energy Environ. Sci.*, 2016, **9**, 962-970.
9. Y. Yang, M. Yang, Z. Li, R. Crisp, K. Zhu and M. C. Beard, *J. Phys. Chem. Lett.*, 2015, **6**, 4688-4692.
10. C. Motta, F. El-Mellouhi, S. Kais, N. Tabet, F. Alharbi and S. Sanvito, *Nat. Commun.*, 2015, **6**, 7.
11. N. J. Jeon, J. H. Noh, W. S. Yang, Y. C. Kim, S. Ryu, J. Seo and S. I. Seok, *Nature*, 2015, **517**, 476-480.
12. N. J. Jeon, J. H. Noh, Y. C. Kim, W. S. Yang, S. Ryu and S. Il Seol, *Nat. Mater.*, 2014, **13**, 897-903.
13. L. Zheng, D. Zhang, Y. Ma, Z. Lu, Z. Chen, S. Wang, L. Xiao and Q. Gong, *Dalton Trans.*, 2015, **44**, 10582-10593.
14. Y. B. Yuan and J. S. Huang, *Acc. Chem. Res.*, 2016, **49**, 286-293.
15. S. Kazim, M. K. Nazeeruddin, M. Graetzel and S. Ahmad, *Angew. Chem. Int. Ed.*, 2014, **53**, 2812-2824.
16. M. Saba, F. Quochi, A. Mura and G. Bongiovanni, *Acc. Chem. Res.*, 2016, **49**, 166-173.
17. J. Xie, Y. Liu, J. Liu, L. Lei, Q. Gao, J. Li and S. Yang, *J. Power Sources*, 2015, **285**, 349-353.
18. G. Niu, X. Guo and L. Wang, *J. Mater. Chem. A*, 2015, **3**, 8970-8980.
19. D. Wang, M. Wright, N. K. Elumalai and A. Uddin, *Sol. Energy Mater. Sol. Cells*, 2016, **147**, 255-275.
20. S. N. Habisreutinger, T. Leijtens, G. E. Eperon, S. D. Stranks, R. J. Nicholas and H. J. Snaith, *Nano Lett.*, 2014, **14**, 5561-5568.
21. M. Zhang, M. Lyu, H. Yu, J.-H. Yun, Q. Wang and L. Wang, *Chem. Eur. J.*, 2015, **21**, 434-439.
22. J. H. Noh, S. H. Im, J. H. Heo, T. N. Mandal and S. I. Seok, *Nano Lett.*, 2013, **13**, 1764-1769.

23. V. D'Innocenzo, A. R. Srimath Kandada, M. De Bastiani, M. Gandini and A. Petrozza, *J. Am. Chem. Soc.*, 2014, **136**, 17730-17733.
24. C. M. Sutter-Fella, Y. Li, M. Amani, J. W. Ager, F. M. Toma, E. Yablonovitch, I. D. Sharp and A. Javey, *Nano Lett.*, 2015.
25. L. Gil-Escrig, A. Miquel-Sempere, M. Sessolo and H. J. Bolink, *J. Phys. Chem. Lett.*, 2015, **6**, 3743-3748.
26. B.-w. Park, B. Philippe, S. M. Jain, X. Zhang, T. Edvinsson, H. Rensmo, B. Zietz and G. Boschloo, *J. Mater. Chem. A*, 2015, **3**, 21760-21771.
27. T. J. Jacobsson, J.-P. Correa-Baena, M. Pazoki, M. Saliba, K. Schenk, M. Graetzel and A. Hagfeldt, *Energy Environ. Sci.*, 2016, **9**, 1706-1724.
28. B. R. Sutherland and E. H. Sargent, *Nat. Photonics*, 2016, **10**, 295-302.
29. M. R. Leyden, L. K. Ono, S. R. Raga, Y. Kato, S. H. Wang and Y. B. Qi, *J. Mater. Chem. A*, 2014, **2**, 18742-18745.
30. P. Luo, Z. Liu, W. Xia, C. Yuan, J. Cheng and Y. Lu, *Acs Appl. Mater. Interfaces*, 2015, **7**, 2708-2714.
31. M. M. Tavakoli, L. Gu, Y. Gao, C. Reckmeier, J. He, A. L. Rogach, Y. Yao and Z. Fan, *Sci. Rep.*, 2015, **5**.
32. M. Xiao, F. Huang, W. Huang, Y. Dkhissi, Y. Zhu, J. Etheridge, A. Gray-Weale, U. Bach, Y.-B. Cheng and L. Spiccia, *Angew. Chem. Int. Ed.*, 2014, **53**, 9898-9903.
33. Y. Zhou, M. Yang, W. Wu, A. L. Vasiliev, K. Zhu and N. P. Padture, *J. Mater. Chem. A*, 2015, **3**, 8178-8184.
34. A. H. Ip, L. N. Quan, M. M. Adachi, J. J. McDowell, J. Xu, D. H. Kim and E. H. Sargent, *Appl. Phys. Lett.*, 2015, **106**.
35. J. J. Chang, H. Zhu, B. C. Li, F. H. Isikgor, Y. Hao, Q. H. Xu and J. Y. Ouyang, *J. Mater. Chem. A*, 2016, **4**, 887-893.
36. B. Cai, W.-H. Zhang and J. Qiu, *Chin. J. Catal.*, 2015, **36**, 1183-1190.
37. Y. Z. Wu, A. Islam, X. D. Yang, C. J. Qin, J. Liu, K. Zhang, W. Q. Peng and L. Y. Han, *Energy Environ. Sci.*, 2014, **7**, 2934-2938.
38. R. G. Niemann, A. G. Kontos, D. Palles, E. I. Kamitsos, A. Kaltzoglou, F. Brivio, P. Falaras and P. J. Cameron, *J. Phys. Chem. C*, 2016, **120**, 2509-2519.
39. T. Oku, in *Solar Cells - New Approaches and Reviews*, ed. L. A. Kosyachenko, InTech, 2015, ch. 3, pp. 77-101.
40. E. T. Hoke, D. J. Slotcavage, E. R. Dohner, A. R. Bowring, H. I. Karunadasa and M. D. McGehee, *Chem. Sci.*, 2015, **6**, 613-617.
41. D. Q. Bi, S. J. Moon, L. Haggman, G. Boschloo, L. Yang, E. M. J. Johansson, M. K. Nazeeruddin, M. Gratzel and A. Hagfeldt, *Rsc Adv.*, 2013, **3**, 18762-18766.
42. T. Leijtens, B. Lauber, G. E. Eperon, S. D. Stranks and H. J. Snaith, *J. Phys. Chem. Lett.*, 2014, **5**, 1096-1102.
43. D. Nanova, A. K. Kast, M. Pfannmoller, C. Muller, L. Veith, I. Wacker, M. Agari, W. Hermes, P. Erk, W. Kowalsky, R. R. Schroder and R. Lovrincic, *Nano Lett.*, 2014, **14**, 2735-2740.
44. S. J. Yoon, K. G. Stamplecoskie and P. V. Kamat, *J. Phys. Chem. Lett.*, 2016, **7**, 1368-1373.
45. T. Salim, S. Sun, Y. Abe, A. Krishna, A. C. Grimsdale and Y. M. Lam, *J. Mater. Chem. A*, 2015, **3**, 8943-8969.
46. S. Gamliel and L. Etgar, *RSC Adv.*, 2014, **4**, 29012-29021.

47. T. A. Berhe, W. N. Su, C. H. Chen, C. J. Pan, J. H. Cheng, H. M. Chen, M. C. Tsai, L. Y. Chen, A. A. Dubale and B. J. Hwang, *Energy Environ. Sci.*, 2016, **9**, 323-356.
48. W. Li, J. Fan, J. Li, Y. Mai and L. Wang, *J. Am. Chem. Soc.*, 2015, **137**, 10399-10405.
49. E. Edri, S. Kirmayer, D. Cahen and G. Hodes, *J. Phys. Chem. Lett.*, 2013, **4**, 897-902.
50. G. Grancini, V. D'Innocenzo, E. R. Dohner, N. Martino, A. R. S. Kandada, E. Mosconi, F. De Angelis, H. I. Karunadasa, E. T. Hoke and A. Petrozza, *Chem. Sci.*, 2015, **6**, 7305-7310.
51. M. Hirasawa, T. Ishihara, T. Goto, K. Uchida and N. Miura, *Physica B*, 1994, **201**, 427-430.
52. F. Brivio, C. Caetano and A. Walsh, *J. Phys. Chem. Lett.*, 2016, **7**, 1083-1087.
53. Y. Yamada, T. Nakamura, M. Endo, A. Wakamiya and Y. Kanemitsu, *J. Am. Chem. Soc.*, 2014, **136**, 11610-11613.
54. Y. Yamada, T. Yamada, P. Le Quang, N. Maruyama, H. Nishimura, A. Wakamiya, Y. Murata and Y. Kanemitsu, *J. Am. Chem. Soc.*, 2015, **137**, 10456-10459.
55. X. Wen, R. Sheng, A. W. Y. Ho-Baillie, A. Benda, S. Woo, Q. Ma, S. Huang and M. A. Green, *J. Phys. Chem. Lett.*, 2014, **5**, 3849-3853.
56. H.-H. Fang, R. Raissa, M. Abdu-Aguye, S. Adjokatse, G. R. Blake, J. Even and M. A. Loi, *Adv. Funct. Mater.*, 2015, **25**, 2378-2385.
57. E. M. Hutter, G. E. Eperon, S. D. Stranks and T. J. Savenije, *J. Phys. Chem. Lett.*, 2015, **6**, 3082-3090.
58. G. Xing, N. Mathews, S. Sun, S. S. Lim, Y. M. Lam, M. Graetzel, S. Mhaisalkar and T. C. Sum, *Science*, 2013, **342**, 344-347.
59. L. Atourki, E. Vega, B. Mari, M. Mollar, H. Ait Ahsaine, K. Bouabid and A. Ihlal, *Appl. Surf. Sci.*, 2016, **371**, 112-117.
60. D. Shi, V. Adinolfi, R. Comin, M. J. Yuan, E. Alarousu, A. Buin, Y. Chen, S. Hoogland, A. Rothenberger, K. Katsiev, Y. Losovyj, X. Zhang, P. A. Dowben, O. F. Mohammed, E. H. Sargent and O. M. Bakr, *Science*, 2015, **347**, 519-522.
61. S. D. Stranks, G. E. Eperon, G. Grancini, C. Menelaou, M. J. P. Alcocer, T. Leijtens, L. M. Herz, A. Petrozza and H. J. Snaith, *Science*, 2013, **342**, 341-344.
62. L. L. Wang, C. McCleese, A. Kovalsky, Y. X. Zhao and C. Burda, *J. Am. Chem. Soc.*, 2014, **136**, 12205-12208.
63. J. S. Manser and P. V. Kamat, *Nat. Photonics*, 2014, **8**, 737-743.
64. K. G. Stamplecoskie, J. S. Manser and P. V. Kamat, *Energy Environ. Sci.*, 2015, **8**, 208-215.
65. M. B. Price, J. Butkus, T. C. Jellicoe, A. Sadhanala, A. Briane, J. E. Halpert, K. Broch, J. M. Hodgkiss, R. H. Friend and F. Deschler, *Nat. Commun.*, 2015, **6**.
66. Y. Yang, D. P. Ostrowski, R. M. France, K. Zhu, J. van de Lagemaat, J. M. Luther and M. C. Beard, *Nat. Photonics*, 2016, **10**, 53-59.
67. B. Doughty, M. J. Simpson, B. Yang, K. Xiao and Y. Z. Ma, *Nanotechnology*, 2016, **27**.
68. M. J. Simpson, B. Doughty, B. Yang, K. Xiao and Y. Z. Ma, *J. Phys. Chem. Lett.*, 2016, **7**, 1725-1731.
69. M. J. Simpson, B. Doughty, B. Yang, K. Xiao and Y.-Z. Ma, *ACS Photonics*, 2016, **3**, 434-442.
70. V. Roiati, E. Mosconi, A. Listorti, S. Colella, G. Gigli and F. De Angelis, *Nano Lett.*, 2014, **14**, 2168-2174.

71. A. M. A. Leguy, P. Azarhoosh, M. I. Alonso, M. Campoy-Quiles, O. J. Weber, J. Z. Yao, D. Bryant, M. T. Weller, J. Nelson, A. Walsh, M. van Schilfgaarde and P. R. F. Barnes, *Nanoscale*, 2016, **8**, 6317-6327.
72. O. Flender, J. R. Klein, T. Lenzer and K. Oum, *Phys. Chem. Chem. Phys.*, 2015, **17**, 19238-19246.
73. A. Marchioro, J. Teuscher, D. Friedrich, M. Kunst, R. van de Krol, T. Moehl, M. Gratzel and J. E. Moser, *Nat. Photonics*, 2014, **8**, 250-255.
74. P. Piatkowski, B. Cohen, F. J. Ramos, M. Di Nunzio, M. K. Nazeeruddin, M. Gratzel, S. Ahmad and A. Douhal, *Phys. Chem. Chem. Phys.*, 2015, **17**, 14674-14684.